Journal of Controlled Release 368 (2024) 66–83

Contents lists available at ScienceDirect

Journal of Controlled Release

journal homepage: www.elsevier.com/locate/jconrel

Dual stimuli-responsive and sustained drug delivery NanoSensoGel formulation for prevention of cisplatin-induced ototoxicity

Neeraj S. Thakur [a], Iulia Rus [a], Ethan Sparks [b], Vibhuti Agrahari [a,*]

[a] Department of Pharmaceutical Sciences, University of Oklahoma Health Sciences Center, Oklahoma City, OK 73117, USA
[b] Department of Integrative Biology, Oklahoma State University, Stillwater, OK 74078, USA

ARTICLE INFO

Keywords:
ROS-responsive nanoparticles
Thermo-responsive hydrogel
Hearing loss
Chemotherapy
Inner ear drug delivery
Long-term release

ABSTRACT

Cisplatin (*Cis*Pt)-induced ototoxicity (CIO) is delineated as a consequence of *Cis*Pt-induced intracellular generation of reactive oxygen species (ROS) which can be circumvented by Bucillamine (BUC; an antioxidant drug with sulfhydryl groups) and Diltiazem (DLT, L-type calcium channel blocker). However, its effective accumulation in the Organ of Corti and cell cytoplasm is desired. Therefore, a biocompatible BUC- and DLT-nanoparticles (NPs)-impregnated dual stimuli-responsive formulation (NanoSensoGel) presented here with ROS- and thermo-responsive properties for the sustained and receptive delivery of drugs. The ROS-responsive polypropylene sulfide- methyl polyethylene glycol-2000 (PPS-mPEG$_{2000}$) polymer was rationally designed, synthesized, and characterized to fabricate BUC- and DLT-loaded PPS-mPEG$_{2000}$-NPs (BUC- and DLT-NPs). The fabricated BUC- and DLT-NPs showed efficient cellular uptake, intracellular delivery, ROS responsiveness, and cytoprotective effect which was characterized using cellular internalization, intracellular ROS, mitochondrial superoxide, and Caspase 3/7 assays on the House Ear Institute-Organ of Corti-1 (HEI-OC1) cells. The composite NanoSensoGel (i.e., ROS-responsive BUC- and DLT-NPs suspended in the thermo-responsive hydrogel) present in a sol state at room temperature and turned to gel above 33°C, which could be essential for retaining the formulation at the target site for long-term release. The NanoSensoGel showed sustained release of BUC and DLT following Fickian release diffusion kinetics. Overall, a novel NanoSensoGel formulation developed in this study has demonstrated its great potential in delivering therapeutics in the inner ear for prophylactic treatment of CIO, and associated hearing loss.

1. Introduction

Cisplatin (*Cis*Pt) is a highly effective antitumor drug generally used in the treatment of solid malignant tumors and, is commonly used to treat several types of cancers such as ovarian, cervical, lung, brain, etc. [1]. However, *Cis*Pt causes severe side effects such as bone marrow depression, nephrotoxicity, and ototoxicity, thus limiting its clinical application as a lifesaving treatment [2]. The incidence of cisplatin-induced ototoxicity (CIO) ranges from 40 to 60% and is more prevalent in children, affecting more than 70% of pediatric patients [3]. *Cis*Pt reaches the inner ear within minutes of systemic treatment and outer hair cells (OHCs) are more severely affected than inner hair cells (IHCs). Thus, CIO results in permanent inner ear cell damage. Hearing loss manifests as progressive, bilateral, and irreversible; therefore, prophylactic, or early treatment is crucial. Though the etiology of CIO remains unclear, investigators have suggested that the ototoxicity is mainly related to the production of reactive oxygen species (ROS) and activation of the apoptotic pathway in the organ of Corti hair cells after *Cis*Pt administration [2,4]. Several strategies have been attempted to develop effective otoprotective methods against cisplatin-induced hearing loss (CIHL) in vitro and in vivo [5–7]. Nonetheless, the anti-tumor effect of *Cis*Pt was also found to be weakened by the systemic administration of those drugs for hearing protection, especially antioxidants [2]. Therefore, establishing a local administration strategy contributes to the otoprotection without affecting the effect of *Cis*Pt treatment [8]. Food and Drug Administration recently approved sodium thiosulfate as preventive medication for hearing impairment caused by *Cis*Pt in pediatric patients and the two trials [SIOPEL 6 (NCT00652132) and COG ACCL0431 (NCT00716976) showed about 50% efficacy [9]. However, other significant adverse effects were reported such as bone pain, cough, high blood pressure, dizziness, pale skin, ulcers, etc. [9,10]. Therefore, there is a critical need for the development of a safe and

* Corresponding author at: College of Pharmacy, 1110 N. Stonewall Avenue, Oklahoma City, OK 73117, USA.
E-mail address: vibhuti-agrahari@ouhsc.edu (V. Agrahari).

https://doi.org/10.1016/j.jconrel.2024.02.005
Received 31 January 2024; Accepted 6 February 2024
Available online 21 February 2024

effective therapeutic option that provides a viable approach to prophylactically treating CIO and CIHL.

*Cis*Pt leads to apoptosis of auditory hair cells via intracellular generation of ROS and free radicals as well as damaging the cell's DNA [11]. The generation of ROS can deplete protective antioxidant molecules in cochlear tissues such as glutathione and antioxidant enzymes. This study investigates the Bucillamine (BUC) (*N*-(2-mercapto-2-methylpropionyl)-L-cysteine); a thiol donor compound used to treat rheumatoid arthritis [12], however, a report shows that BUC prevents the CIO and protects sensory hair cells from *Cis*Pt [13]. In addition, the oxidative environment results in cytochrome *c* release from the mitochondria, which leads to an increase in calcium release from the endoplasmic reticulum [14]. The calcium release then causes a massive cytochrome *c* release activating the apoptotic cascade. Furthermore, it has been observed that ROS species can open these channels hence leading to an increase in cytosolic calcium levels [15]. ROS-dependent oxidative degradation of cochlear tissue may allow lipid peroxidation, which can increase calcium influx and apoptosis in cells of the cochlea. Thus, calcium influx is considered a major contributor to apoptosis. Recent in vivo studies in mice have suggested that the intratympanic (IT) administration of diltiazem (DLT), an L-type calcium channel blocker may reduce the concentration of calcium precipitates at the basolateral membrane of the OHCs [16]. Thus, another active molecule studied in this investigation is Diltiazem.

The inner ear consists of two entangled organs: the vestibular apparatus, which is the organ of balance, and the cochlea, the organ of hearing. The inner ear is a very isolated organ located in the temporal bone and protected by many physiological barriers and the most challenging target for the treatment of inner ear diseases is the delivery of therapeutic agents without damaging the integrity or function of the inner ear [17,18]. Currently, systemic or local delivery is widely used in the treatment of various inner ear diseases [19]. However, the existence of the blood-cochlear barrier and limited blood flow to the cochlea prevent the delivery of drugs from the blood to the inner ear and often results in sub-therapeutic drug concentrations [20]. Therefore, the local application of formulations onto the round window membrane (RWM) is a promising way of targeting drugs to the inner ear, which can directly deliver therapeutic agents into it bypassing the blood-cochlear barrier. Intratympanic administration by injection of the drug inside the middle ear cavity is a safe and common route of administration used in the clinic [21].

Nanotechnology-based systems have shown great potential because of their nanoscale size and can permeate through the RWM easily [22]. ROS-responsive berberine-loaded multicomponent (lecithin, DSPE-PEG_{2000}, and PPS_{120}-OH) nanoparticles were developed to ameliorate noise-induced hearing loss [23]. Gu et al. reported the astaxanthin-loaded polypropylene sulfide nanoparticles to combat CIO [24]. However, the liquid nature of nanoformulations and their low bio-retention need a combined approach for the delivery of nanoformulations to the inner ear. Among several strategies, the hydrogel systems are able to accomplish the high bio-retention of nanoformulations onto the RWM [25,26]. Once a drug crosses the RWM into the inner ear provides a reservoir to continuously release encapsulated therapeutic molecules into the inner ear. Therefore, a combination of nanotechnology with a hydrogel approach can address the current limitations of low bio-retention in the inner ear and offer a suitable option to develop a minimally invasive, sustained, and targeted drug delivery system. Here, we developed and investigated an inner ear-targeted drug delivery system based on the combination of ROS-responsive BUC/DLT loaded PPS-$mPEG_{2000}$-NPs and a thermo-responsive hydrogel collectively called NanoSensoGel. In this approach, the hydrogel has promoted prolonged residence due to its sol-to-gel transition at body temperature, and bio-adhesive properties, and PPS-$mPEG_{2000}$-NPs holding capacity for sustained release of the therapeutic drugs. The ROS-responsive BUC/DLT-loaded PPS-$mPEG_{2000}$-NPs has ability to release the drugs upon *Cis*Pt-induced ROS generation to protect the inner hair cells from apoptosis and cell death.

2. Materials and methods

2.1. Materials

Diltiazem hydrochloride (DLT, TCI), methoxy polyethylene glycol-$_{2000}$ ($mPEG_{2000}$, TCI), *p*-toluenesulfonyl chloride (TosCl, TCI), 1,8-Diazabicyclo[5.4.0]undec-7-ene (DBU, Thermo Fischer) propylene sulfide (TCI), potassium thioacetate (TCI), 2,2′-azino-bis (3-ethylbenzothiazoline-6-sulfonic acid (ABTS, TCI), cis-Diammineplatinum(II) Dichloride (*Cis*Pt, TCI), Chlorpromazine (CPZ, TCI), methyl-β-cyclodextrin (MβCD, TCI), Amiloride (AML, TCI), Genistein (GNT, TCI) and Fluorescein 5-Isothiocyanate (FITC, TCI), triethylamine (TEA, Fischer Chemical), Methanol (Fischer Chemical), dichloromethane (DCM, Fischer Chemical), acetonitrile (ACN, Fischer Chemical), Sodium sulfate (Fischer Chemical), sodium chloride (Fischer Chemical), Trolox (Thermo Fischer), Ammonium Persulfate (APS, MP Biomedicals), propidium iodide (PI, MP Biomedicals) Coumarin-6 (Thermo Fischer), HOECHST 33342 (Tocris Biosciences), 2′,7′-Dichlorofluorescein 3′,6′-diacetate ($DCFH_2$-DA, Thermo Fischer), Poloxamer 188 (P188, Alfa Aesar), Carbomer 940 (C940, Spectrum) and hydrochloric acid (HCl) were purchased from Fischer Scientific, USA. Diethyl ether, Toluene, Tetrahydrofuran, Iodine, Poloxamer 407 (P407), and anhydrous DCM were purchased from Millipore Sigma, USA. Bucillamine was purchased from eNovation LLC, USA. The cell culture media, reagents, and phosphate buffer saline (PBS) were procured from Millipore Sigma, USA. MitoSOX™ Cat: M36008, assay kit was received as a kind gift from Invitrogen, USA.

2.2. Synthesis of polypropylene sulfide-methyl polyethylene glycol $_{2000}$ (PPS-$mPEG_{2000}$) polymer and Bucillamine (BUC) and diltiazem (DLT) loaded PPS-$mPEG_{2000}$ nanoparticles (NPs)

The PPS-$mPEG_{2000}$ polymer was synthesized using a previously reported functionalization and conjugation strategy [27–30]. The detailed methodology has been furnished in the supporting information section S1. Further, polymeric nanoparticles (NPs) were synthesized using the nanoprecipitation method [31]. Briefly, in two separate microcentrifuge tubes containing 15 and 10 mg PPS-$mPEG_{2000}$ polymer, bucillamine (BUC, 2.25 mg) and diltiazem; (DLT, 1.5 mg) were taken, respectively. The content of each tube was dissolved in acetone (1 mL; organic phase). The organic phase of each tube was dropwise added to the separate centrifuge tube containing deionized water (1.5 mL) under the sonication and continued to sonicate for 15 s. The colloidal solution was then transferred to a glass vial and allowed to stir for 2 h at room temp and 150 RPM. The residual organic solvent was evaporated using rotavapor. The synthesized BUC-PPS-$mPEG_{2000}$-NPs (BUC-NPs) and DLT-PPS-$mPEG_{2000}$-NPs (DLT-NPs) were characterized using dynamic light scattering (DLS), nanoparticle tracking analysis (NTA; NanoSight-NS300; Malvern Inc, UK), transmission electron microscopy (TEM; JEOL 2010F, Japan) and stored at 4 °C. The concentrations of the encapsulated BUC and into respective NPs were determined using standard methods (detailed quantification assay procedures have been incorporated in the SI sections S3 and S4). The percent encapsulated efficiency (EE%) and percent drug loading (DL%) were calculated using following equations:

$$\mathrm{EE}(\%) = \frac{C}{C_0} \times 100 \quad (1)$$

$$\mathrm{DL}(\%) = \frac{C}{P_0} \times 100 \quad (2)$$

Where, C is the concentration of the drug into the NPs, C_0 is the initial drug concentration, and P_0 is the concentration of added polymer.

The storage stability of synthesized NPs was determined for up to 2

months. Note: The optimization of polymer-to-drug concentrations was performed at different polymer-to-drug ratios utilizing the design of experiment – central composite design (DoE-CCD) prior to the final synthesis of the NPs. The detailed table of optimization of NPs preparation using CCD is furnished in the supporting information section S5.

2.3. Free radical scavenging assay

Briefly, the aqueous solutions of APS (245 mM, 10 μL) and ABTS 7 mM, 1000 μL) were mixed well and incubated at room temperature overnight in dark. The resulting solution ($ABTS^+$ radical solution) was diluted up to 20 mL. Different concentrations of standard antioxidant Trolox (6.25 to 400 mM) were prepared in PBS. The 20 μL solutions of standards (Trolox) and test samples (BUC-NPs, DLT-NPs, and BUC/DLT-NPs) were added to the separate wells in a multi-well plate ($n = 3$). Deionized water was used as the control group. In each well containing standard samples, test samples, and control groups, 180 μL of $ABTS^+$ radical solution was added. The plate was then incubated for 5 min at room temperature in dark and the absorbance was recorded at 734 nm using a multi-well plate reader (Synergy 2, BioTek, USA). The inhibition of $ABTS^+$ radical was calculated in terms of decolorization (%) using the following equation [32]:

$$\text{Decolorization } (\%) = \left(\frac{\text{Control Abs} - \text{Sample Abs}}{\text{Control Abs}}\right) \times 100 \quad (3)$$

The standard equation was derived using standard samples (SI section S6). Further, the samples' antioxidant capacities were determined in terms of equivalent Trolox concentration (mg/mg) using the following equation:

$$\text{Trolox} - \text{eq } (mg/mg) = \left(\frac{\text{Sample decolorization } (\%) - \text{b}}{\text{a}}\right) \div \textit{Sample concentration } (mg/mL) \quad (4)$$

Where b is the intercept of the standard graph, and a is the slope of the regression line.

2.4. In vitro assessments using HEI-OC1

2.4.1. Cellular uptake

In the colloidal solution of blank PPS-mPEG$_{2000}$ NPs, 1 mg of coumarin-6 (C-6) was added, and the mixture was stirred overnight (150 RPM) at RT in a closed vial. The resulting colloidal solution containing C-6 loaded PPS-mPEG$_{2000}$ NPs (C-6-NPs) was then centrifuged at 2000 rpm for 5 min to remove the unloaded C-6. The supernatant containing C-6-NPs was used as a stock solution for the study. In a culture flask, the House Ear Institute-Organ of Corti-1 (HEI-OC1) cells were grown for 3 days at 33 °C in complete growth media (recipe see in SI section S7) and collected in a centrifuge tube after washing with fresh media. The cells were seeded overnight in two 24 well plate (1×10^5 cells per well in 400 μL media). The culture media of each well was replaced with the media containing C-6-NPs (1:100; 10 μL C-6-NPs stock diluted up to 10 mL using culture media). The plates were kept at 33 °C, 5% CO_2 for incubation. After 1 h, the media from the first-row wells were removed, and the cells were counterstained using HOECHST 33342 (400 μL, 0.5 μg/mL solution in DPBS, incubation 5–10 min at room temperature). The cells were then washed using fresh DPBS and analyzed under a fluorescence microscope (Revolve, ECHO, San Diego, CA; λex/λem for C-6 and HOECHST 33342 were 460/501 and 350/461 nm, respectively). The similar procedure was followed for five more consequent columns (2–6) after 2, 3, 4, 5, and 6 h of incubation, respectively. After image capturing, the cells of each well were lysed using radioimmunoprecipitation assay (RIPA) buffer (400 μL per well; for the recipe please see SI section S8). The lysed cell suspension from each well was transferred in a microcentrifuge tube and the dye content was extracted using DCM. Briefly, 500 μL DCM was added in each tube and vortexed for at least 5 min. The tubes were then centrifuged at 2,000 RPM for 5 min and the DCM content from the bottom of the tubes was collected in separate tubes. The DCM content was evaporated by keeping the tubes open in a fume hood overnight. The residual of each tube was then dissolved in 100 μL methanol and the fluorescence intensity of the methanolic solution was recorded using a multi-well plate reader (Synergy 2, BioTek, USA; λex/λem for C-6 was 457/501 nm). To confirm the cellular uptake pathway, the cells were grown as discussed above and treated with different uptake inhibitors (CPZ, MβCD, AML, and GNT) at a concentration of 30 μg/mL for 1 h before adding C-6-NPs. After 4 h of incubation, washing, lysis, extraction, and preparing methanolic solution, the fluorescence intensity was recorded using a multi-well plate reader as discussed above.

2.4.2. Cell viability and biocompatibility assay

A standard MTT assay was performed to evaluate the cell viability to determine the biocompatibility of the developed formulations. The HEI-OC1 cells were seeded to the 96 well plate at a concentration 2×10^4 cells per well and incubated for 60 h at 33 °C (under 5% CO_2). The cells in each column were then incubated with the media (100 μL) having different treatment components (Column 1: Blank medium, Column 2: 20 μM *Cis*Pt containing medium, Column 3: BUC-NPs equivalent to 20 μM of BUC, Column 4: DLT-NPs equivalent to 20 μM of DLT and Column 5: BUC/DLT-NPs equivalent to 10 μM of BUC and DLT; $n = 8$). The cells were incubated for 36 h at 33 °C under 5% CO_2. After washing the cells using fresh media, 100 μL MTT containing media (10 μL, 5 mg/mL MTT reagent in 90 μL growth medium; MTT assay kit, Roche, Germany) was added to each well and incubated for another 5 h. The solubilizing buffer (100 μL) in each well was added and the plate was incubated overnight. The absorbance at 570 nm was recorded using a multi-well plate reader (Synergy-2, BioTek, USA).

2.4.3. CisPt-induced cytotoxicity inhibition study

The HEI-OC1 cells were seeded in a 96 well plate (2×10^4 cells per well) and incubated for 60 h. Each well in a column was treated with the same treatment regimen. The columns were first treated with 100 μL media containing different treatment components (Column 1: Blank medium, Column 2: Blank medium, Column 3: BUC-NPs equivalent to 20 μM of BUC, Column 4: DLT-NPs equivalent to 20 μM of BUC, Column 5: BUC/DLT-NPs equivalent to 10 μM of BUC and DLT, Column 6: 20 μM BUC Solution, Column 7: 20 μM DLT solution, Column 8: BUC and DLT solutions 10 μM of each $n = 8$)) and incubated for 5 h. Then 100 μL media containing *Cis*Pt (40 μM, final concentration in each well 20 μM) was added in each column except 'column 1' and incubated for 36 h. The cells were then washed using fresh media and 100 μL MTT reagent containing growth media (90 μL media and 10 μL MTT reagent) was added to each well. After 5 h of incubation, the solubilizing buffer (100 μL) was added to each well and the plate was incubated overnight. After incubation, the absorbance was recorded at 570 nm using a multi-well plate spectrophotometer (Synergy 2, BioTek, USA).

For live dead-cell analysis, the cells were seeded in a 6 well plate (2×10^5 cells/well) and incubated overnight. The cells were treated with different treatment components and then *Cis*Pt exactly as mentioned above. After completion of incubation with *Cis*Pt, the cells were washed carefully using DPBS (2×) and incubated with propidium iodide (1 μg/mL in DPBS) for 15 min in dark at room temperature. The cells were then washed using DPBS (1×) and counterstained with HOECHST-33342 (0.5 μg/mL solution in DPBS) and FITC (0.4 μg/mL in DPBS) by incubating them for 10 min in dark at room temperature. The cells were carefully washed using fresh DPBS (2×) and fresh DPBS was added to each well. The cells were observed under a digital fluorescence microscope (Revolve, ECHO, San Diego, CA, λex/λem for PI, FITC, and HOECHST 33342 were 535/615, 495/519, and 350/461 nm, respectively).

2.4.4. The intracellular ROS scavenging capability study

The ROS scavenging capability of developed BUC-NPs and DLT-NPs was determined using $DCFH_2$-DA assay [33]. Briefly, the HEI-OC1 cells were seeded in a 96 well plate (2×10^4 cells per well) and incubated for 48 h. After treatment with different regimens (Column 1: Blank medium, Column 2: Blank medium, Column 3: BUC-NPs equivalent to 20 μM of BUC, Column 4: DLT-NPs equivalent to 20 μM of BUC, Column 5: BUC/DLT-NPs equivalent to 10 μM of BUC and DLT, Column 6: 20 μM BUC Solution, Column 7: 20 μM DLT solution, Column 8: BUC and DLT solutions 10 μM of each) the cells were incubated for 5 h and then 100 μL medium containing 40 μM *Cis*Pt was added in each column (except in column 1). The cells were then incubated for 24 h. After washing with fresh media cells were incubated with 100 μL $DCFH_2$-DA solution (10 μM) for 30 min. The cells were then washed carefully (2×, DPBS) and lysed using 100 μL RIPA buffer in each well. The lysed cell suspension from each well was transferred in a microcentrifuge tube and the dye content was extracted using DCM as discussed above (cellular uptake section 2.4.1). After DCM evaporation, the residue of each tube was dissolved in methanol (100 μL) and the fluorescence intensity of the methanolic solution was recorded using a multi-well plate fluorescence spectrophotometer (Synergy 2, BioTek, USA; λex/λem for DCF were 485/530 nm).

To confirm the ROS scavenging capability of various treatment regimens the treated cells were visualized using fluorescence microscopy. Briefly, HEI-OC1 cells were seeded in 6 well plates (2×10^5 per well) and incubated overnight. The seeded cells in each well were incubated with 2 mL media containing different treatment regimens (well 1: Blank medium, well 2: Blank medium, well 3: BUC-NPs equivalent to 20 μM of BUC, well 4: DLT-NPs equivalent to 20 μM of DLT, well 5: BUC/DLT-NPs equivalent to 10 μM of BUC and DLT) for 5 h. The cells were then treated with 40 μM *Cis*Pt (20 μM, final concentration in culture medium) except well 1. After 24 h of incubation, the cells were washed with fresh media and incubated with freshly prepared $DCFH_2$-DA reagent (10 μM working solution in the culture media) for 30 min. The $DCFH_2$-DA-containing media was then carefully removed, and the cells were washed using fresh culture media (1×) and DPBS (2×). The cells were counterstained using HOECHST 33342 (0.5 μg/mL solution in DPBS, incubation 5–10 min at room temperature). Then cells were washed with fresh DPBS and analyzed under a fluorescence microscope (λex/λem for DCF and HOECHST 33342 were 480/530 and 350/461 nm, respectively).

2.4.5. Determination of mitochondrial superoxide scavenging using MitoSOX assay

The ability of developed BUC-NPs and DLT-NPs to scavenge the mitochondrial superoxide was determined using MitoSOX assay. Briefly, the HEI-OC1 cells were seeded in a 96 well plate (2×10^4 cells/well) and incubated for 60 h. The cells were treated with various test regimens (Column 1: Blank medium, Column 2: Blank medium, Column 3: BUC-NPs equivalent to 20 μM of BUC, Column 4: DLT-NPs equivalent to 20 μM of BUC, Column 5: BUC/DLT-NPs equivalent to 10 μM of BUC and DLT) and incubated for 5 h. The cells were then treated with 20 μM *Cis*Pt (final concentration, except in column 1). The treated cells were incubated for 24 h and then washed using fresh media (2×). After washing, the cells were incubated with MitoSOX reagent according to the manufacturer's protocol (MitoSOX™ Cat: M36008, Invitrogen, USA). After washing with DPBS (2×), the cells of each well were lysed using 100 μL RIPA buffer. The dye content from each well was then extracted using DCM following the procedure discussed above (cellular uptake section 2.4.1) and dissolved in methanol (100 μL). The fluorescence intensity of the methanolic solution was recorded using a multi-well plate fluorescence spectrophotometer (Synergy 2, BioTek USA; λex/λem for MitoSOX were 510/580 nm).

To confirm the superoxide generation and scavenging effect the treated cells were visualized using fluorescence microscopy. Briefly, HEI-OC1 cells were seeded in a 6 well plates (2×10^5 per well) and incubated overnight. The seeded cells were treated with test regimens (well 1: Blank medium, well 2: Blank medium, well 3: BUC-NPs equivalent to 20 μM of BUC, well 4: DLT-NPs equivalent to 20 μM of DLT, well 5: BUC/DLT-NPs equivalent to 10 μM of BUC and DLT) for 5 h. The cells were then treated with *Cis*Pt (20 μM, final concentration in culture medium except well 1). After 24 h of incubation with *Cis*Pt, the cells were washed with fresh media and treated with freshly prepared MitoSOX reagent according to the manufacturer's protocol. The MitoSOX-containing growth media from the wells were removed and the cells were counterstained using HOECHST 33342. The cells were then washed with fresh DPBS and analyzed under a fluorescence microscope. λex/λem for MitoSOX and HOECHST 33342 were 510/580 and 350/461 nm, respectively.

2.4.6. Caspase 3/7 assay

The effect of BUC-NPs and DLT-NPs on *Cis*Pt-induced Caspase 3/7 activation and further apoptosis was determined by the Caspase 3/7 assay. Briefly, Caspase 3/7 activation in different treatment groups, in 96 well plate the HEI-OC1 cells were seeded (2×10^4 cells/well) and treated the same as mentioned above (cytotoxicity inhibition section 2.4.3). After CisPt treatment and incubation, the cells were stained with FLICA according to the manufacturer's protocol. The cells were then lysed using 100 μL RIPA buffer and the dye content was extracted using DCM (see cellular uptake section 2.4.1 for detailed procedure). The DCM content was evaporated, and the dye content was dissolved in 100 μL methanol. The fluorescence intensity of the methanolic solution was recorded using a multi-well plate fluorescence spectrophotometer (Synergy 2, BioTek, USA; λex/λem for FLICA were 480/520 nm). The fluorescence microscopy study was done to confirm the apoptosis study. Briefly, HEI-OC1 cells were seeded in 6 well plates (2×10^5 per well) and incubated overnight. The seeded cells were treated with the test regimens and *Cis*Pt subsequently the same as mentioned in the cytotoxicity inhibition section 2.4.3. After 24 h of incubation, the cells were washed with fresh media and treated with freshly prepared Fluorescent Labeled Inhibitor of Caspases (FLICA) reagent according to the manufacturer protocol (CaspaTag Caspase 3,7 In Situ Assay Kit Cat#APT423, Millipore Sigma, USA). After staining with FLICA the cells were counterstained using HOECHST 33342. The cells were then washed with fresh DPBS and analyzed under a fluorescence microscope. (λex/λem for FLICA and HOECHST 33342 were 480/520 and 350/461 nm, respectively).

2.4.7. Western blot analysis

After the treatment endpoint, cells were washed with ice-cold PBS and incubated with 100 μl mixture of 2X blue dye (90 μL, for recipe see SI section S9) and β-mercaptoethanol (10 μL) for 1 min at room temperature. The cells were collected using sterile cell scraper in microcentrifuge tube. The samples were centrifuged for 10 sec (1000 rpm) and heated for 5 min at 100 °C. The supernatant was transferred to fresh sterile tubes and stored at −20 °C for further use [34]. After running the samples in SDS-PAGE (4–15% Mini-PROTEAN® TGX™ Precast Protein Gels, BIO-RAD), samples were transferred to the PVDF membrane using Trans-Blot® Turbo™ Transfer System (BIO-RAD). The membrane was blocked using nonfat dried milk (5%) in TBS-T containing Tween 20 (0.1%) at room temperature for 1 h. After washing, the membranes were incubated with respective assay primary antibodies; anti-p-AKT (#4060, 1:1000), anti-AKT (#4685, 1:1000), anti-Phospho p38(#4511, 1:1000), p38 (#8690, 1:1000), anti-ERK1/2 (#4695, 1:1000), and anti-pERK1/2 (Thr202/Tyr204, #9101S) (all from cell signaling technologies) diluted in nonfat dried milk (1.5%) in TBS-T, overnight at 4 °C. The membranes were then washed using TBS-T and incubated further with goat anti-mouse (#92632210, Li-Cor, 1:2500) secondary antibodies for 1 h. The bands corresponding to target expressions were imaged by ChemiDoc Imaging System (BIO-RAD).

2.5. Formulation of thermo-responsive hydrogel (NanoSensoGel) and its physicochemical characterization

Thermo-responsive hydrogels are more effective with enhanced bio-retention to RWM, injectability, and long-term effect for CIO. The thermo-responsive hydrogel formulation was prepared by dissolving P407 (24%, *w/v*), P188 (15% w/v), and C940 (0.1% w/v) using a modification of the cold method as described earlier [35]. Briefly, NanoSensoGel was prepared in using the thermo-responsive hydrogel in the cold colloidal solution of BUC/DLT-NPs (10 mL) and keeping it at 4 °C for overnight. NanoSensoGel was characterized for the Sol-gel transition temperature and time by the tube inversion method [36]. Further, the samples of NanoSensoGel were characterized using Scanning Electron Microscopy (SEM; NEON 40 EsB, FE-SEM, Carl Zeiss AG, Germany) to confirm the structural characteristics of sol and gel states. Briefly, the NanoSensoGel present in sol and gel states were individually snap-freeze by dipping them in the liquid nitrogen (−196 °C). The freeze samples were then lyophilized (FreeZone® Triad™ Freeze Dry System, Labconco, USA) and analyzed under the SEM.

2.6. In vitro release kinetics of NanoSensoGel

The release study of the BUC and DLT from the NanoSensoGel was performed using 24 well plate and inserts with 8 μm size at the bottom (Transwell®, Costar®, Corning, USA) while PBS (pH 7.4, Sigma, USA) was used as the receiving medium. The NanoSensoGel (200 μL, containing BUC/DLT-NPs final concentration 75 μg/mL BUC and DLT) and free BUC/DLT-Gel (200 μL, containing 200 μg/mL BUC and DLT) were loaded in separate trans well inserts ($n = 3$) and kept at 37 °C for 15 min. The PBS (1 mL) maintained at 37 °C was then added to each well containing the hydrogel insert. The wells were carefully sealed using parafilm and the plate was kept at 37 °C. The samples (100 μL) were drawn at 1, 3, 6, 12, 24, 72, 120, and 168 h from the receiving media. The volume of the receiving media was compensated by adding an equal amount of fresh media. The collected samples were analyzed using Ellman's and HPLC methods to quantify BUC and DLT, respectively. The release kinetics of BUC and DLT from both hydrogels were calculated using the Korsmeyer-Peppas model (Eq. (5)) [37].

$$\frac{M_t}{M_\infty} = k_1 t^n \tag{5}$$

Where, M_t is the mass of the drug released at time t; M_∞ is the mass of the total drug; k_1 is the structural and geometric characteristics of dosage form related constant; n is the release mechanism exponent.

2.7. Stability of BUC and DLT in NanoSensoGel

The stability of BUC and DLT in the NanoSensoGel was studied at 25 and 37 °C in PBS buffer pH 7.4. The NanoSensoGel formulation (1 mL) was kept at 25 and 37 °C and the samples (100 μL) were drawn every 24 h for up to 8 days. The drugs from the NanoSensoGel were extracted using DCM. After evaporating the DCM, the BUC and DLT residues were dissolved in 100 μL 0.1 M PBS and methanol, respectively. The quantitative analyses of BUC and DLT contents in the samples were done using Ellman's and HPLC methods, respectively as described in SI sections S3 and S4.

2.8. Determination of cytoprotective effect of NanoSensoGel

The effect of NanoSensoGel formulation on *Cis*Pt-exposed HEI-OC1 cells was determined using an MTT assay [38]. Briefly, the cells were seeded in 24 a well plate (1×10^5 cells/well) and incubated for 36 h. Each column was treated with different regimens (Column 1: untreated control, Column 2: *Cis*Pt only, Column 3: NanoSensoGel equivalent to 20 μM of BUC and DLT, Column 4: 100 μL Free BUC/DLT-Gel, Column 5: BUC/DLT-NPs equivalent to 10 μM of BUC and DLT, Column 6: 10 μM of Free BUC and DLT Solution). The cells were first treated with the respective test formulation and incubated for 5 h. The *Cis*Pt solution was then added in each column except column 1 and the plate was incubated for another 48 h. After incubation, the growth media from each well were aspirated and new media containing MTT reagent were added. After 5 h incubation, the solubilization buffer was added to each well, and the plate was further incubated overnight. The content of each well was transferred in a 96 well plate and the absorbance was recorded at 570 nm. [Note: the gel formulations were administered using 24 well plate inserts with 8 μm size at the bottom (Transwell®, Costar®, Corning, USA)].

2.9. Software and statistical analysis

DOE-CCD tool was utilized for optimization of the preparation of NPs using JMP pro 16 software (SAS, NC, USA). Chemical structures were drawn using ChemDraw 20.1.1 (ChemOffice, PerkinElmer, USA). MestReNova −14.1.2 (Masterlab Research, Spain) software was used for NMR analysis. The statistical analysis of data was carried out through ANOVA (one−/two-way) using GraphPadPrizm 9 (San Diego, USA). The tests were validated using Šidák's multiple comparison post-hoc test where $p < 0.05$ was considered as significantly different. The graphs and figures were drawn using GraphPad Prizm 9, Origin Pro 9, ChemDraw 20.1.1, and Biorender.com.

3. Results and discussion

3.1. Synthesis of ROS-responsive PPS-mPEG2000 amphiphilic polymer

The amphiphilic nature of a polymer is a unique feature that helps to assemble the polymeric units as the nanoparticles (NPs) in the aqueous media without any supplementary addition of surfactant. The hydrophobic units come together and make the core of the particle; however, the hydrophilic units tend to arrange towards the hydrophilic media. Thus, the amphiphilic units are eventually arranged as NPs having a hydrophobic core and hydrophilic surface [39,40]. Therefore, PPS-$mPEG_{2000}$ amphiphilic polymer was successfully synthesized with both hydrophilic and hydrophobic properties in a single molecule in three steps (**Fig. S3a)**. Here, sulfide bonding is introduced in the rationally developed polymer that is highly prone to cleave in presence of in situ ROS providing the stimuli-responsive release property to the synthesized NPs [30,41]. A simple thiol-thiol interaction method was utilized to synthesize the PPS-$mPEG_{2000}$ amphiphiles. After the SH-group functionalization of both PPS and $mPEG_{2000}$ polymers, both were mixed in 1:1 ratio for the synthesis of PPS-$mPEG_{2000}$ amphiphilic polymer. The successful synthesis was evidenced by NMR analysis (**Fig. S3b**). Mechanistically, the S^- group of one SH-containing molecule (either PPS or mPEG-SH) acts as a nucleophile that attacks the sidechain containing -SH group of the second molecule (either mPEG-SH or PPS) and attached through the S—S (disulfide bond) by releasing the electron [42].

3.2. Synthesis and characterization of bucillamine (BUC) and diltiazem (DLT) loaded PPS-$mPEG_{2000}$ nanoparticles (NPs)

The PPS-mPEG NPs to deliver the BUC and DLT into the inner ear were established because of their ability to high drug encapsulation, expected targeted delivery efficacy, and stimuli (ROS) responsiveness. The stimuli-responsive behavior of NPs enables the release of drugs when required (upon generation of ROS) at the target site. This property is highly beneficial in the elimination of undesired drug effects, moreover, the long-term release can significantly reduce the dosing frequency. PPS-$mPEG_{2000}$ copolymer was utilized to synthesize BUC- and DLT-loaded PPS-$mPEG_{2000}$-NPs (BUC-NPs and DLT-NPs). The amphiphilic nature of PPS-$mPEG_{2000}$ units allowed them to assemble as NPs in an aqueous media with a hydrophobic core and hydrophilic surface. Prior to the final synthesis of NPs, the effect of the ratio of polymer to

drug concentration was optimized using the design of experiment-central composite design (DoE-CCD) (See SI section S5). It was observed that the polymer concentration and corresponding drug concentration significantly affect the size, PDI, drug encapsulation efficiency, and drug loading in synthesized NPs. To synthesize BUC-NPs, the optimized polymeric concentration with the smallest size, lowest PDI, maximum encapsulation, and highest drug loading was found to be 15 mg/mL with a corresponding BUC concentration of 15% *w*/w (Fig. 1**a**). Similarly, the optimal concentrations of polymer and drug were found to be 10 mg/mL and 15 (% *w*/w), respectively, to synthesize DLT-NPs (Fig. 1**b**). Using the optimized conditions, the synthesis of BUC-NPs and DLT-NPs was successfully achieved utilizing the nanoprecipitation method [43,44]. After the addition of the organic phase (acetone) containing PPS-mPEG$_{2000}$ polymer and drugs, the clear water turned into a milky colloidal solution which did not show any sign of large phase separation or large particle precipitation. This primary observation confirmed the nanoprecipitation of polymer into deionized water followed by nanoparticle self-assembly. After the evaporation of the organic solvent, no significant change in the appearance of the colloidal solution was observed which primarily confirmed the stable NPs preparation.

The size of the NPs was determined by dynamic light scattering (DLS) analysis which showed the average sizes of BUC-NPs, and DLT-NPs, ~107.1 ± 2.92 and 98.8 ± 2.06 nm, respectively (Fig. 1**c & g**). The polydispersity index (PDI) <0.3 confirmed that most of the NPs have the same size (monodispersed). The size and shape of the NPs were further

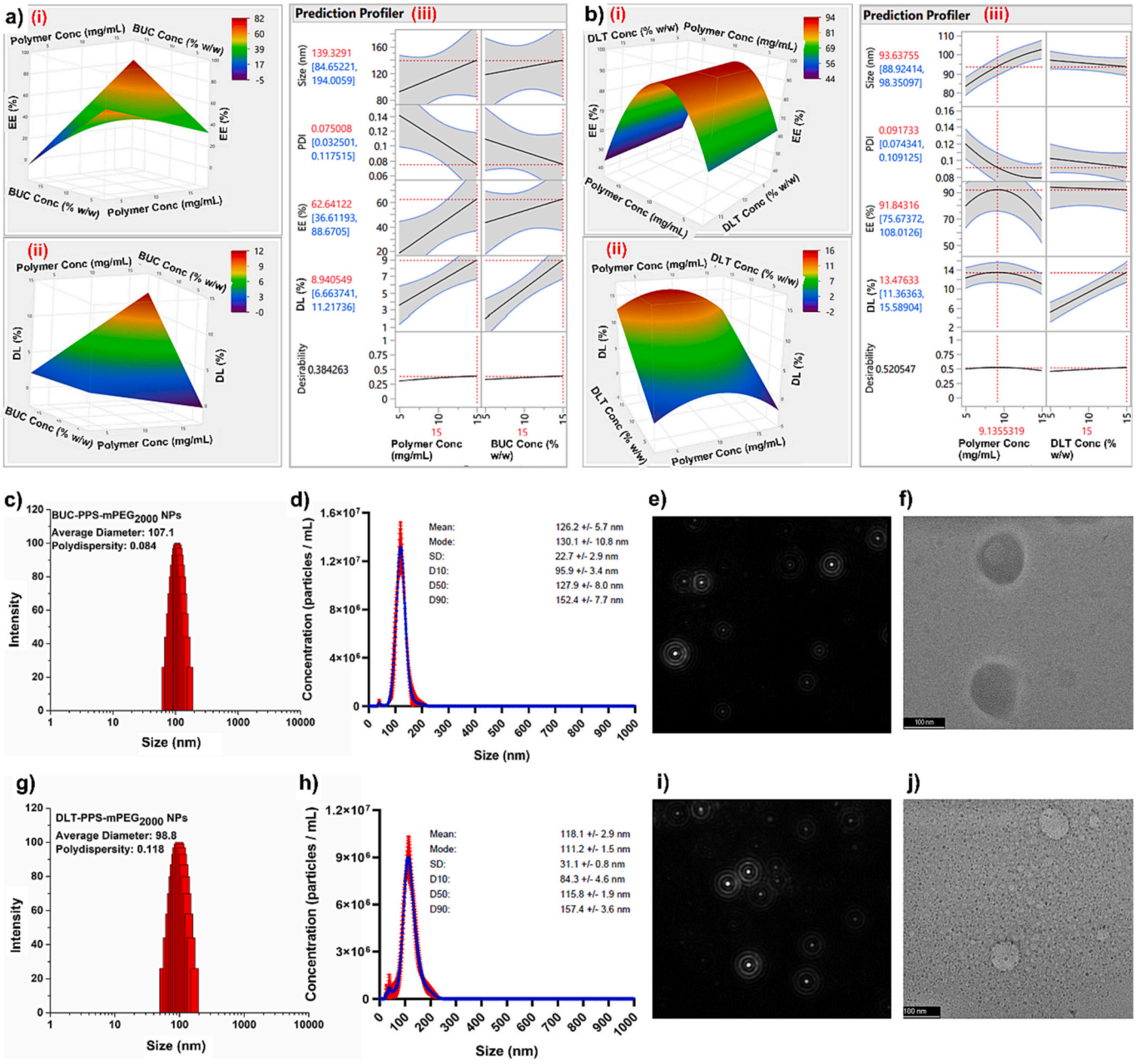

Fig. 1. (a-b) DoE-CCD optimization graphs for the synthesis of **(a)** BUC-NPs and **(b)** DLT-NPs. The corresponding figures (i), (ii), and (iii), represent the encapsulation efficiency (EE%), drug loading (DL %), and prediction profiler, respectively. **(c-j)** Size and morphology analysis of BUC-NPs and DLT-NPs. **(c)** Size distribution of BUC-NPs analyzed by DLS, **(d)** size distribution of BUC-NPs analyzed by nanoparticle tracking analysis (NTA), **(e)** visual image of BUC-NPs under NTA, **(f)** TEM image of BUC-NPs showing spherical shape (scale 100 nm), **(g)** size distribution of DLT-NPs analyzed by DLS, **(h)** size distribution of DLT-NPs analyzed by NTA, **(i)** visual image of DLT-NPs under NTA, **(j)** TEM image of DLT-NPs showing spherical shape (scale 100 nm).

analyzed using nanoparticle tracking analysis (NTA). Both the NP preparations appeared spherical and, the D10/D50/D90 values of BUC- and DLT-NPs were found to be 95.9 ± 3.4/127.9 ± 8.0/152.4 ± 7.7 and 84.3 ± 4.6/115.8 ± 1.9/157.4 ± 3.6 nm, respectively (Fig. 1**d & h**). The D10, D50, and D90 values are defined as the points on the distribution curve below which 10, 50, and 90% particles fall, respectively. Further, morphological analysis of developed NPs using NTA and TEM confirmed the spherical shape and the size of ~100 nm (Fig. 1**e, f, i & j**). The drug encapsulation/drug loading efficiencies of the BUC and DLT in the respective NPs were found to be 55.54 ± 6.17/8.05 ± 0.77 and 88.52 ± 3.78/13.13 ± 0.40%.

The stability of the formulations was further evaluated to establish their long-term storage at cold temperature in deionized water. The synthesized NPs were stored at 4 °C and their size and PDI using DLS were recorded at different time intervals for up to 2 months. There were no significant changes in the size and PDI values were observed (Fig. 2). Thus, it may be categorical that the synthesized NPs were highly stable for >60 days at 4 °C storage. It is well characterized that the PEGylated dispersant layer on the surface of the NPs is responsible for their stabilization [45]. Herein, the hydrophobic moiety (PPS) of the amphiphilic polymer (PPS-mPEG$_{2000}$) assembled as the core and the hydrophilic units (mPEG$_{2000}$) present on the surface of the NPs. The hydrophilic mPEG$_{2000}$ molecules formed a dispersant layer which is accountable for the nanoparticle stabilization. Besides the storage stabilization, the mPEG$_{2000}$ layer is responsible for the longer plasma stability in vivo via inhibition of biomolecular corona effect [46].

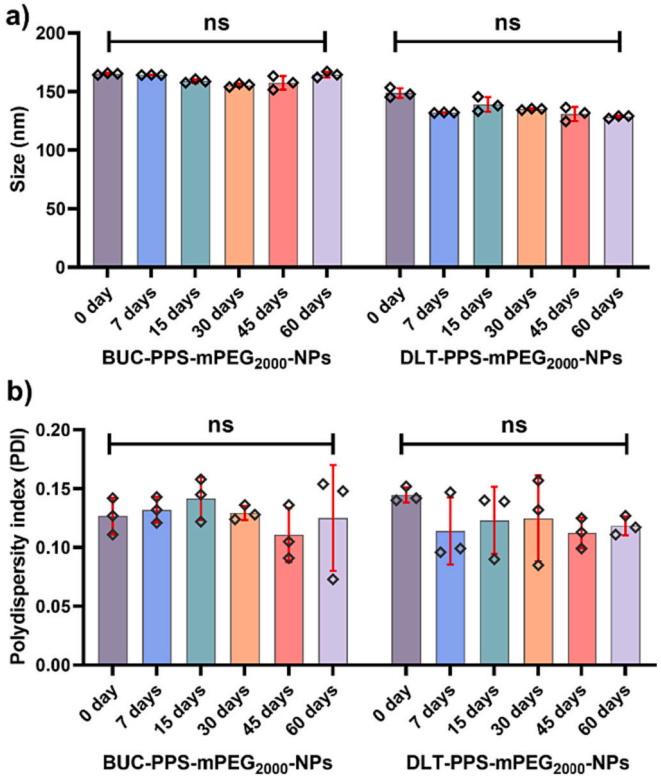

Fig. 2. Storage stability of BUC-NPs and DLT-NPs at 4 °C in terms of structural integrity using (a) size and (b) polydispersity index (PDI) as markers and studied at different time intervals after preparation (0, 7, 15, 30, 45, and 60 days). There was no significant difference in the size and PDI values observed in both NP preparations. (n = 3, data was analyzed using two-way ANOVA for each group and compared using Šidák's multiple comparisons of each group. ns = not significant).

3.3. Antioxidant activity and stimuli-responsive property of developed NPs

The antioxidant activities of the developed PPS-mPEG$_{2000}$-NPs were determined by their percent decolorizing potential of 2,2′-azino-bis (3-ethylbenzothiazoline-6-sulfonic acid (ABTS^{+} free radical scavenging) and equivalent concentration to Trolox (standard) (Fig. 3**a**). The ABTS^{+} free radical scavenging capability of BUC-NPs and BUC/DLT-NPs were found to be significantly higher compared to DLT-NPs. The results suggested that the BUC-NPs had radical scavenging activity, however, DLT-NPs didn't have the same. The combination of equal concentrations of BUC/DLT-NPs showed similar scavenging activity as BUC-NPs which confirmed the free radical scavenging activity only arises because of the presence of BUC. Overall, the developed BUC-NPs were found to be highly beneficial in neutralizing reactive free radicals from the media and acting as antioxidants. Thus, the use of these NPs could play a significant role in reducing the oxidative stress of *Cis*Pt in the inner ear by scavenging the generated ROS and further reducing CIO. However, to achieve the ROS scavenging effect at the cellular level, the BUC must reach the cell cytoplasm. Therefore, the cellular internalization study of PPS-mPEG$_{2000}$-NPs needs to be evaluated to confirm the delivery of loaded BUC in the cells. Further, to confirm the ROS responsiveness of developed NPs, the colloidal solution of NPs was spiked with H_2O_2 (30 μM) at room temperature. After 30 min of incubation, the turbid colour of the solution turned to clear, Moreover, the NTA analysis of NPs solution before and after H_2O_2 addition suggested that the concentration of the NPs in the solution after the incubation with H_2O_2 was significantly reduced (Fig. 3**b-d**). These results suggested that the H_2O_2 was responsible for the dissociation of sulfide bonds and NPs assembly subsequently. Thus, the colour of the solution turned clear after the addition of H_2O_2. Expectedly, the PPS-mPEG$_{2000}$-based NPs could be highly sensitive to intracellular ROS and can release the drugs specifically if the stimuli are present in the environment. Thus, these designed NPs could be ideal for the ROS-responsive release of drugs.

3.4. Cellular uptake, internalization, and distribution of PPS-mPEG$_{2000}$ NPs

The intended effect of the drugs is highly associated with their cellular uptake and intracellular distribution. In order to determine the cellular uptake and intracellular distribution of the NPs, the emission of the nanoparticle tagged with the fluorescent Coumarin−6 (C-6) was measured in the HEI-OC1 using fluorescence microscopy. The quantitative analysis of the fluorescence in the cells treated with the C-6-PPS-mPEG$_{2000}$-NPs was done at different time intervals up to 6 h. It was observed that the cellular uptake of the C-6-PPS-mPEG$_{2000}$-NPs was time-dependent, and the maximum uptake was observed at 6 h. However, there was no significant difference in C-6 fluorescence between 5 and 6 h observed which confirmed that >90% cellular uptake of NPs achieved within 5 h of incubation **(**Fig. 4**a)**. Moreover, the microscopy of the cells also confirmed the cellular uptake of C-6-PPS-mPEG$_{2000}$-NPs within 6 h and showed uniform intracellular distribution and retention of internalized NPs (Fig. 4**b**). Further, the molecular pathway of cellular internalization of developed NPs was determined by inhibiting the specific pathway. The cells that were treated with Chlorpromazine (CPZ; clathrin-dependent endocytosis inhibitor) prior to NPs incubation showed significantly low fluorescence intensities compared to the untreated cells. However, other pathway inhibitors such as cholesterol-dependent lipid rafting inhibitor (methyl-β-cyclodextrin; MβCD) [47], caveolin-mediated endocytosis inhibitor (Genistein; GNT), and Macropinocytosis inhibitor (Amiloride; AML) did not show significant uptake inhibition (Fig. 4**c**). These results suggested that the PPS-mPEG$_{2000}$-NPs uptake follows clathrin-dependent endocytosis mechanism. The cellular uptake is expected to be via a clathrin-mediated cellular internalization route because of the mPEG$_{2000}$ surface functionality of the developed PPS-mPEG$_{2000}$-NPs. The cellular internalization process of PEG-

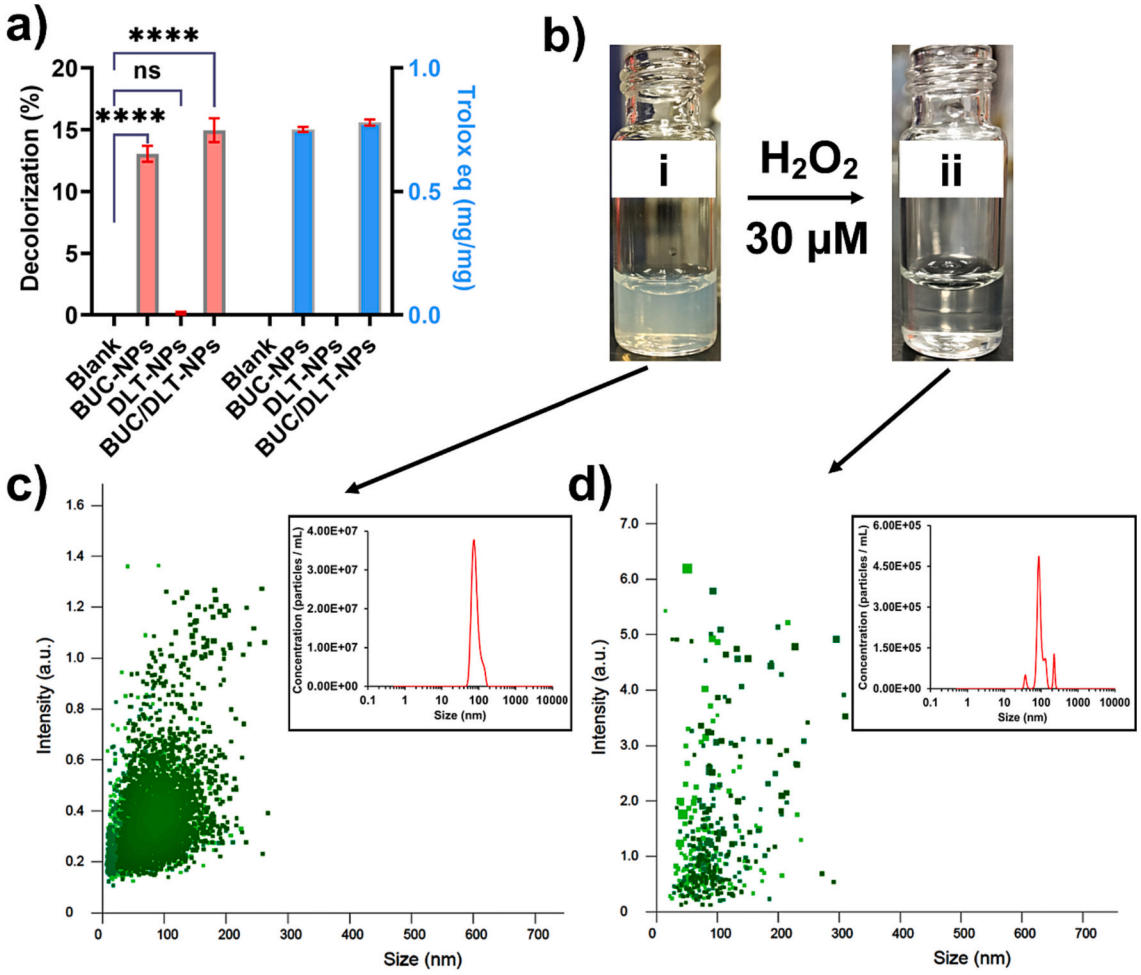

Fig. 3. **(a)** The graph shows the effect of developed NP preparations against $ABTS^{+}$ free radicals in terms of % decolorization effect and the corresponding activity equivalent to the Trolox standard. The BUC-NPs and the combination of BUC/DLT-NPs have significantly higher radical scavenging activity compared to DLT-NPs alone. (The groups were compared using two-way ANOVA using Šidák's multiple comparisons post-hoc test. "$n = 3$", Asterisks: **** $p \leq 0.0001$; ns = not significant). **(b)** effect of H_2O_2 on the PPS-$mPEG_{2000}$-NPs. Images 'i' and 'ii' show the visual appearance of the colloidal solution before and after H_2O_2 addition, respectively. **(c)** NTA analysis of the colloidal NP solution before H_2O_2 addition (after 100× dilution) shows the intensity of PPS-$mPEG_{2000}$-NPs. Inset graph showing the concentration of the NPs in the solution. **(d)** NTA analysis of the colloidal NP solution after H_2O_2 addition (after 100× dilution) shows the intensity of NPs. Inset graph showing the concentration of the NPs in the solution.

functionalized NPs with size <200 nm is highly characterized in the literature and the most common cell internalization pathway of PEGylated NPs is the clathrin-mediated pathway [43,48–51]. Thus, we can expect here the PPS-$mPEG_{2000}$-NPs up-taken by HEI-OC1 cells via a clathrin-dependent route that has been schematically presented in **Fig. 4d**.

3.5. *Biocompatibility of BUC-NPs and DLT-NPs with cells, and their cytoprotective effect under oxidative stress*

Biocompatibility of the therapeutic biomaterial played a significant role in the preclinical and clinical translational investigations. Thus, the biocompatibility of developed BUC-NPs (20 μM equivalent to BUC) and DLT-NPs (20 μM equivalent to DLT) with HEI-OC1 cells was evaluated while using *Cis*Pt (20 μM) as the positive control. The results of the MTT assay suggested that HEI-OC1 cells that were treated with either BUC-NPs and DLT-NPs or with both, did not show any significant difference in cell growth compared to untreated cells (negative control). However, a significant cytotoxic effect was observed on HEI-OC1 cells that were treated with *Cis*Pt only (positive control) (**Fig. 5a**).

To study the cytoprotective effect of developed NPs, the cells were treated with various test regimens as discussed in the method section. It was observed that the cells that were treated with BUC-NPs and BUC/DLT-NPs showed significant growth by countering the cytotoxic effect of *Cis*Pt. However, there was no significant cytoprotective effect was observed in the groups that were treated with DLT-NPs, BUC solution, DLT solution, and BUC/DLT solution (**Fig. 5b**). The non-cytoprotective effect of DLT herein corroborates the previous reports where they reported no effect of DLT on *Cis*Pt-induced cell toxicity [52]. The study confirms that the cytoprotective effect is mainly associated with ROS scavenging by BUC. Moreover, the free BUC solution also does not show a cytoprotective effect because of the hindrance of free BUC cell uptake by the cells. Thus, the delivery of BUC by PPS-$mPEG_{2000}$-NPs is highly desirable to counter the *Cis*Pt-induced oxidative stress. This finding corroborates the results of both the antioxidant ($ABTS^{+}$ radical scavenging) assay and cell uptake study and confirms that BUC-NPs is the main regimen that is needed to protect against *Cis*Pt-induced cytotoxicity. The overall study suggested that both BUC-NPs and DLT-NPs were highly biocompatible with HEI-OC1 cells. However, only BUC-NPs could be referred to as main NPs with cytoprotective capability against CIO.

Furthermore, to confirm the cytoprotective effect of BUC-NPs and BUC/DLT-NPs, the live-dead staining study of HEI-OC1 cells was done after treatment with various regimens. The results suggested that the HEI-OC1 cells that were treated with NPs regimens containing BUC

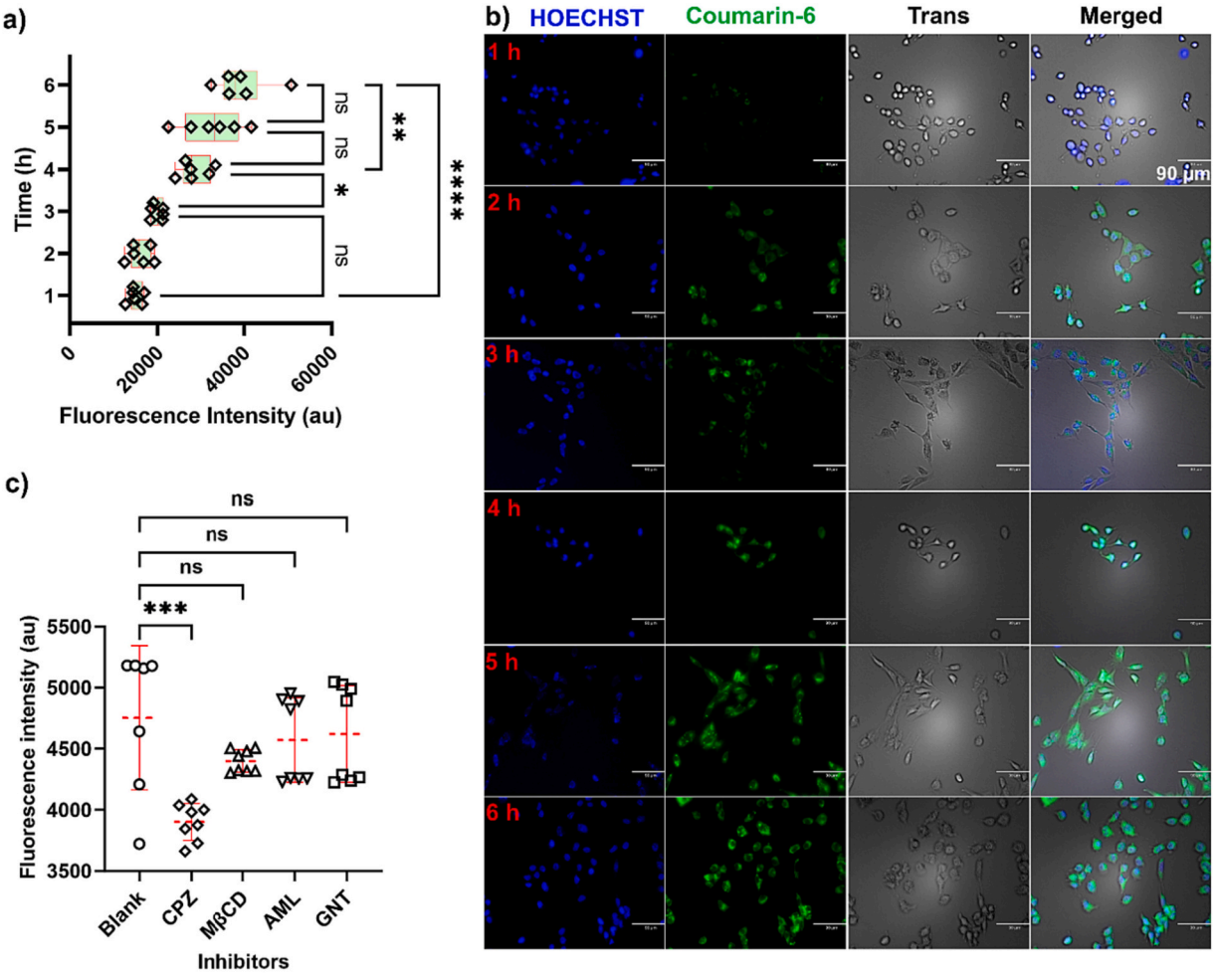

(caption on next page)

Fig. 4. Cellular uptake and intracellular distribution study of NPs using C-6-PPS-mPEG$_{2000}$-NPs. **(a) Time required for significant cellular internalization:** The graph shows the fluorescence intensities of the extracted media after the lysis of the cells that were incubated with C-6 loaded NPs for different times (1, 2, 3, 4, 5, and 6 h) (λex = 460 ± 40 nm, λem = 528 ± 20 nm). The cells showed significant cellular internalization after 4 h of incubation compared to 1 h. The highest internalization was observed at 6 h of incubation. However, no significant difference in fluorescence intensity between 5 and 6 h suggests >90% cellular uptake within 5 h. Therefore, the optimal incubation time for cellular internalization of PPS-mPEG$_{2000}$-NPs resides between 5 and 6 h. (The groups were compared using one-way ANOVA using Šidák's multiple comparison post-hoc test. 'n = 6', Asterisks: **** $p < 0.0001$; ** $p \leq 0.005$; * $p \leq 0.05$; ns = not significant). **(b) Fluorescence microscopy to confirm the cellular uptake and intracellular distribution:** The fluorescence microscopy images of the cells incubated with C-6-PPS-mPEG$_{2000}$-NPs at different time intervals (1–6 h). Each row shows four images; (1) HOECHST 33342 stained nuclei (λex = 358 nm, λem = 461 nm), (2) C-6 fluorescence in the respective cells (λex = 480 nm, λem = 502 nm), (3) cells under transmit light and, (4) merged image. The fluorescence of coumarin in the cells was observed at different time intervals. (Scale 90 μm). These graphs and images suggest that PPS-mPEG$_{2000}$-NPs were able to be successfully internalized and distributed into HEI-OC1 cells. **(c) Elucidation of cellular internalization pathway:** The graph showing the internalization of C-6-PPS-mPEG$_{2000}$-NPs after treatment with specific internalization pathway inhibitors. Here, Chlorpromazine(CPZ; clathrin-dependent endocytosis inhibitor) shows significant endocytosis inhibition. However, Methyl-β-Cyclodextrin (MβCD; cholesterol-dependent lipid rafting inhibitor), Amiloride (AML; Macropinocytosis inhibitor), and Genistein (GNT, Caveolin mediated endocytosis inhibitor). (The groups were compared using one-way ANOVA using Šidák's multiple comparison post-hoc test. 'n = 8' Asterisks: *** $p < 0.001$; ns = not significant). **(d) Molecular mechanism of internalization:** Clathrin-mediated internalization is a plausible molecular mechanism of cellular internalization of C-6-PPS-mPEG$_{2000}$-NPs. The depicted figure describes all steps involved in this process which include, (1) receptor recognition and attachment, (2) formation, stabilization, and release of clathrin-coated vesicle, (3i) uncoating, (4) endosome recognition and fusion, and (5) release in the cytoplasm. (The template scheme of clathrin-mediated cell uptake was created using https://biorender.com/).

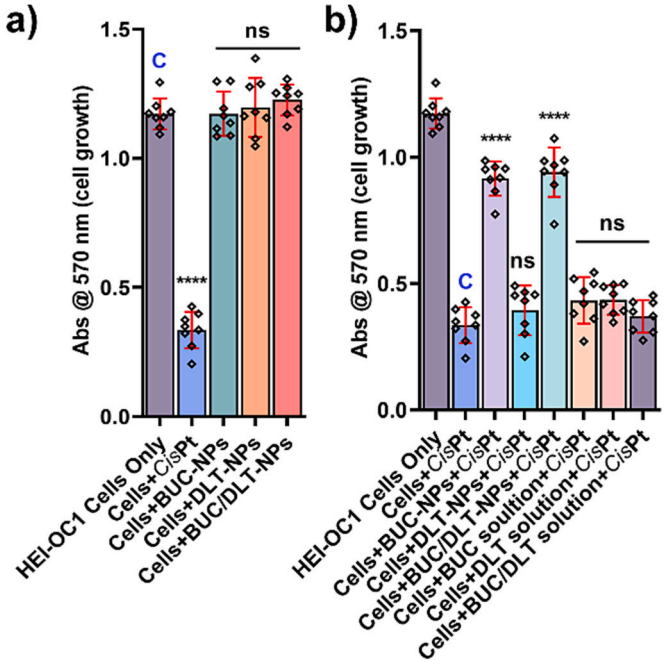

Fig. 5. Biocompatibility of developed NPs and cytoprotective effect of various treatment regimens against *Cis*Pt induced cytotoxicity. The names of test groups in this figure can be abbreviated as BUC-NPs, DLT-NPs, and BUC/DLT-NPs. **(a)** Graph showing the growth of HEI-OC1 cells with various developed NPs and *Cis*Pt (positive control). Cells that were incubated with the BUC-NPs, DLT-NPs, and with both NPs did not show significant growth reduction compared to untreated cells (negative control, denoted as "C"). However, the cells that were treated with *Cis*Pt show significant growth reduction (cytotoxicity). Thus, the developed NPs were highly biocompatible with the HEI-OC1 cells. **(b)** Graph showing the effect of various treatment regimens (NPs and free drug solutions) on the stressed HEI-OC1 cells. The significant cytoprotective effect in HEI-OC1cells against *Cis*Pt (positive control, denoted as "C") can be observed in that were treated with BUC-NPs and BUC/DLT-NPs. No significant cytoprotective effect observed in the cells that were treated with DLT-NPs and free drug solutions. Therefore, BUC-NPs highly desirable to achieve the cytoprotective effect against *Cis*Pt-induced cytotoxicity. "Note: the data of HEI-OC1 cells only and cells+*Cis*Pt were same in Fig. 5**a** and 5b." (The groups were compared using one-way ANOVA using Šidák's multiple comparisons post-hoc test. 'n = 8', Asterisks: **** $p \leq 0.0001$; ***, $p \leq 0.0005$; **, $p \leq 0.001$; ns = not significant). (For interpretation of the references to colour in this figure legend, the reader is referred to the web version of this article).

(BUC-NPs and BUC/DLT-NPs) not show significant PI staining representing more survival capability (no significant difference than the untreated control group; Fig. 6**a, c,** & **e**). Nevertheless, the HEI-OC1 cells that were treated with DLT-NPs showed significant propidium iodide (PI) staining referred to as dead (similar to the *Cis*Pt positive control group) (Fig. 6**b** & **d**). Thus, it may be confirmed that BUC-NPs have a high cytoprotective effect against *Cis*Pt-induced cytotoxicity in HEI-OC1 cells.

3.6. *Determination of intracellular pathways involved in CisPt-induced CIO and the protective effect of developed formulations*

As the study results suggest significant cytoprotective efficacy of BUC-NPs against *Cis*Pt-induced cytotoxicity, it is important to understand the mechanistic aspects of the effect where BUC is involved in the protection of the cells. It has been established that the *Cis*Pt induces ROS generation in the cell cytoplasm and the generation of superoxide in the mitochondria. These ROS are further responsible for inducing oxidative stress in the cells which leads to caspase activation, cell apoptosis, and ultimately cell necrosis. Therefore, the effect of BUC-NPs and DLT-NPs on *Cis*Pt-induced ROS generation, mitochondrial superoxide generation, and caspase 3/7 activation was evaluated.

3.6.1. *ROS scavenging effect*

The effect of BUC-NPs and DLT-NPs on cellular ROS scavenging was determined using $DCFH_2$-DA assay. $DCFH_2$ oxidation assay is the most characterized technique for the qualitative and quantitative analysis of intracellular ROS (Fig. 7**a**) [53,54]. The cells preincubated with test regimens and *Cis*Pt were incubated with $DCFH_2$-DA for 30 min. The extracted medium of lysed cells was then characterized using a fluorescence spectrophotometer for the quantitative determination of intracellular ROS (the higher the fluorescence intensity higher the ROS quantity) (Fig. 7**b**). The comparative fluorescence intensities of test groups suggested that the HEI-OC1 cells that were pretreated with BUC-NPs and BUC/DLT-NPs before *Cis*Pt showed significantly lowered fluorescence intensity compared to *Cis*Pt treated cells (positive control). However, other groups that were treated with DLT-NPs and free drugs (BUC and DLT) before *Cis*Pt, showed significant fluorescence intensities. This study suggested that the BUC-NPs were able to scavenge ROS significantly in *Cis*Pt-exposed cells. Although free BUC (BUC solution and BUC/DLT solution) showed ROS scavenging effect, there was significantly higher ROS generation observed compared to untreated control which could lead the cells ultimately in the apoptotic state. This might be due to moderated cellular internalization of free BUC compared to BUC entrapped in NP. The results were confirmed using fluorescence microscopy of the cells after the treatment with BUC-NPs, DLT-NPs, and BUC/DLT-NPs then *Cis*Pt, subsequently. The

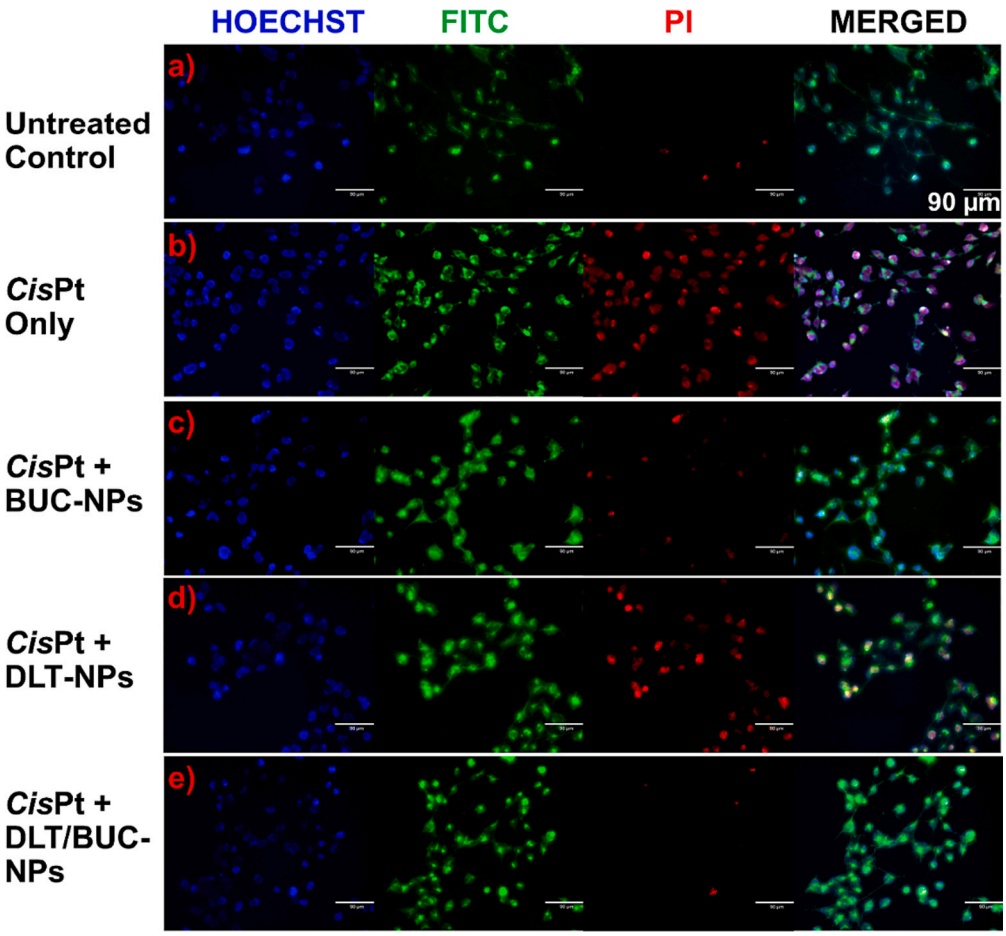

Fig. 6. Live-dead cell imaging of the HEI-OC1 cells after different treatments. Here, the first column associated with each group shows HOECHST 33342 stained nucleus of each cell (irrespectively live/dead). Second column shows all cells stained by FITC dye (irrespectively live/dead). Third column shows the nucleus of the cells stained by PI (dead cells only). Fourth column shows merged images corresponding to the respective group in the same row. (Scale 90 μm). In each group, all cells showed HOECHST 33342 and FITC staining, however, differ in PI staining. **(a) Untreated control:** Only a few cells gained PI stain suggest presence of most of the live cells in the group. **(b) Cells + *Cis*Pt:** Almost all cells gained PI stain suggest presence of most of the dead cells in the group. **(c) Cells + BUC-NPs + *Cis*Pt**: The cells were incubated with BUC-NPs before the *Cis*Pt-exposure. Most of the cells were not stained with PI stain suggest significant live cells are present compared to group 'b'. **(d) Cells + DLT-NPs + *Cis*Pt**: The cells were incubated with DLT-NPs before the *Cis*Pt-exposure. Most of the cells were stained with PI stain suggest significant dead cells are present compared to group 'a' and no significant difference of live cells compared to group 'b'. **(e) Cells + BUC/DLT-NPs + *Cis*Pt:** The cells were incubated with BUC/DLT-NPs before the *Cis*Pt-exposure. Most of the cells were not stained with PI stain suggest significant live cells are present compared to group 'b'.

fluorescence imaging showed significant fluorescence generation in the cells that were not treated with BUC-entrapped NPs (Fig. 7**c**). Thus, BUC-NPs alone or in combination with DLT-NPs have demonstrated as highly efficient as ROS scavengers in HEI-OC1 cells and could be beneficial to protect CIO. Since significant ROS generation was observed in the cells that were treated with free BUC and DLT (BUC and DLT solutions only), we did not consider these treatment groups for further studies.

3.6.2. Mitochondrial superoxide scavenging evaluation using MitoSOX™ assay

As demonstrated in the above experiments, the ROS scavenging effect and subsequent cell survival of HEI-OC1 cells are highly correlated. It was reported that the *Cis*Pt induces the generation of superoxide from the mitochondria in the cells that lead to the initiation of cell apoptosis and necrosis subsequently [55,56]. The ability of developed NP preparations to scavenge the mitochondrial superoxide was evaluated using the MitoSOX™ assay. The MitoSOX™ is a dye that specifically interacts with superoxide generated in mitochondria and flourishes red upon excitation at 510 nm (Fig. 8**a**). It was observed that the cells treated with BUC-containing NPs (BUC-NPs and BUC/DLT-NPs) did not show significant fluorescence compared to the untreated control. This suggested that the BUC that was delivered by PPS-mPEG$_{2000}$-NPs was able to scavenge generated mitochondrial superoxide and protect the cells by inhibiting cell apoptosis. Nevertheless, the cells that were treated with *Cis*Pt and DLT-NPs only showed high fluorescence which suggests the significant presence of superoxide in the cells that could lead them to the apoptotic state (Fig. 8**b**). Similar results were observed in fluorescence microscopy, where the cells that were treated with BUC-based NPs (BUC-NPs and BUC/DLT-NPs) showed lower MitoSOX fluorescence compared to those treated with DLT-NPs before treating with *Cis*Pt (Fig. 8**c**). Thus, BUC-NPs alone or in combination with other NPs could be an appropriate treatment regimen to efficiently prevent CIO.

3.6.3. Determination of apoptosis via caspase 3/7 activation

The apoptotic cell death is primarily associated with the activation of caspases. Caspase 3/7 activation in cells is considered a universal indicator of apoptotic cell death irrespective of the stimulus [57]. Thus, the Fluorescent Labeled Inhibitor of Caspases (FLICA) based assay was performed to evaluate the activation of caspase 3/7 in NPs treated and untreated cells. The FLICA (FAM-DEVD-FMK) is mainly composed of three sequences (1) a fluorescent dye (FAM: Carboxyfluorescein), (2) a

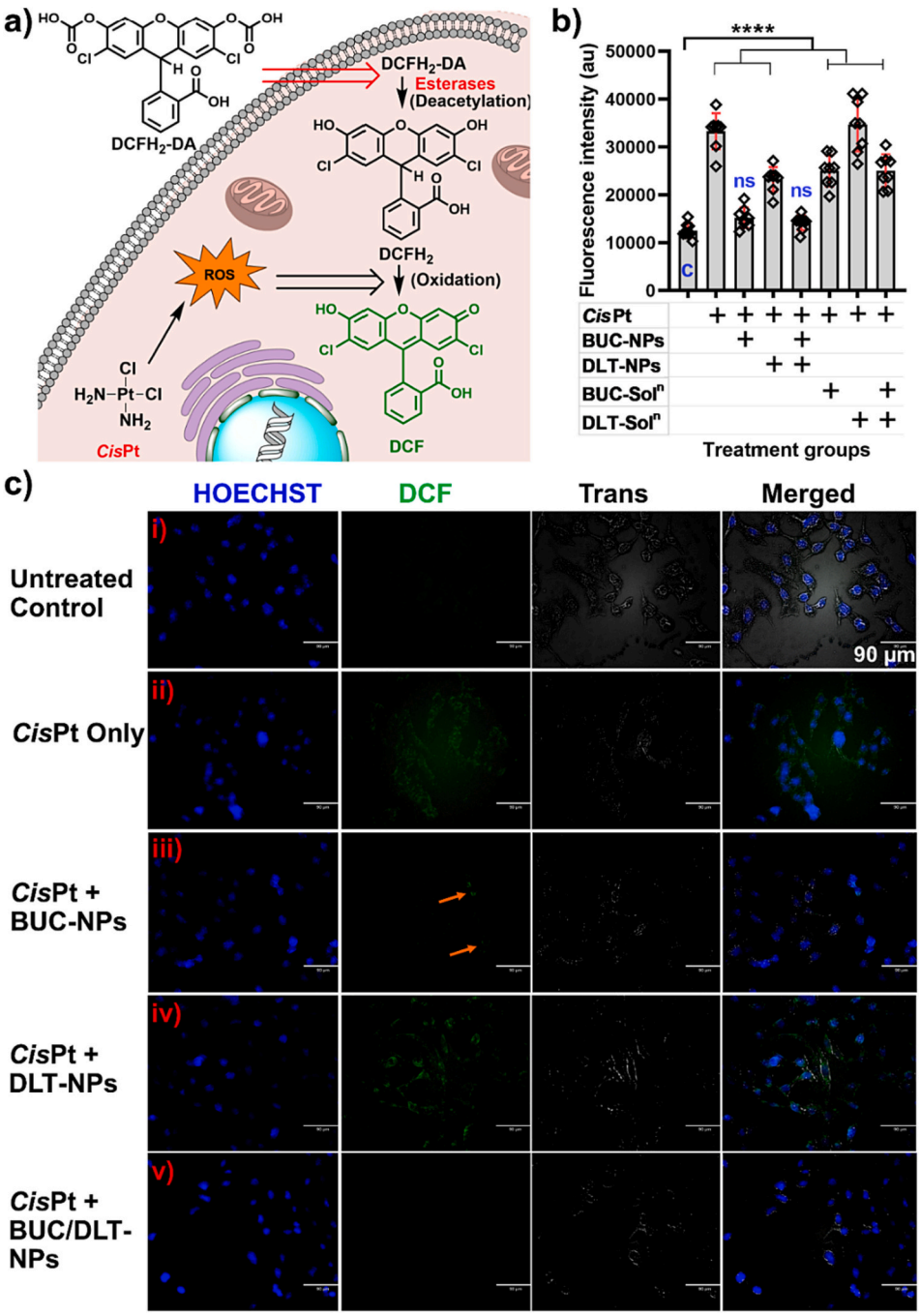

Fig. 7. The $DCFH_2$-DA assay for the detection of intracellular ROS. **(a) Mechanism of $DCFH_2$-DA assay:** The conversion of nonfluorescent $DCFH_2$-DA to fluorescent DCF into the cell cytoplasm by ROS-induced oxidation. $DCFH_2$-DA reached inside the cell is first converted to $DCFH_2$ (nonfluorescent) by esterases and then subsequently oxidized to DCF (fluorescent) via ROS if present in the cytoplasm. This fluorescence inception can be noted as confirmation of ROS generation in the cytoplasm which can be responsible for the oxidative stress of the cells. **(b) Quantitative comparison of fluorescence generation:** The graph shows fluorescence intensities of DCF in various treatment groups. The higher fluorescence in a group can be directly correlated with the higher generation of ROS in the respected group. All treatment groups (except BUC-NPs and BUC/DLT-NPs treated) showed significantly higher fluorescence intensities compared to the untreated control group (denoted by the 'c'). (The groups were compared using one-way ANOVA using Šidák's multiple comparison post-hoc test. '$n = 8$', Asterisks: **** $P < 0.0001$; ** $P \leq 0.005$; ns = not significant). *Inference: by CisPt induction.* **(c) Fluorescence microscopy imaging of cells after treatment and $DCHF_2$-DA staining:** The fluorescence microscopy images of various groups to observe the DCF-associated fluorescence generation. The first column shows the HOECHST 33342-stained nuclei of each cell irrespective of the presence or absence of ROS. The second column (DCF) shows the fluorescence of the DCF produced after oxidation of DCFH by ROS (significantly high fluorescence is associated with higher ROS concentration). The third column shows cells under transmittance light. The fourth column shows merged images. (Scale 90 µm). Here, (i) the untreated cells did not show much DCF fluorescence suggestlow ROS generation, (ii) *Cis*Pt-only treated cells showed significant DCF fluorescence suggest high ROS generation, (iii) BUC-NPs treated cells with subsequent *Cis*Pt treatment group shows a little amount of ROS (DCF fluorescence) because the ROS scavenging capability of BUC-NPs. (iv) DLT-NPs treated cells with subsequent *Cis*Pt treatment show a significant amount of ROS (DCF fluorescence) because of the low ROS scavenging capability of DLT-NPs. (v) BUC/DLT-NPs treated cells with subsequent *Cis*Pt treatment did not show significant DCF fluorescence (ROS concentration) because of the ROS scavenging capability of BUC/DLT-NPs.

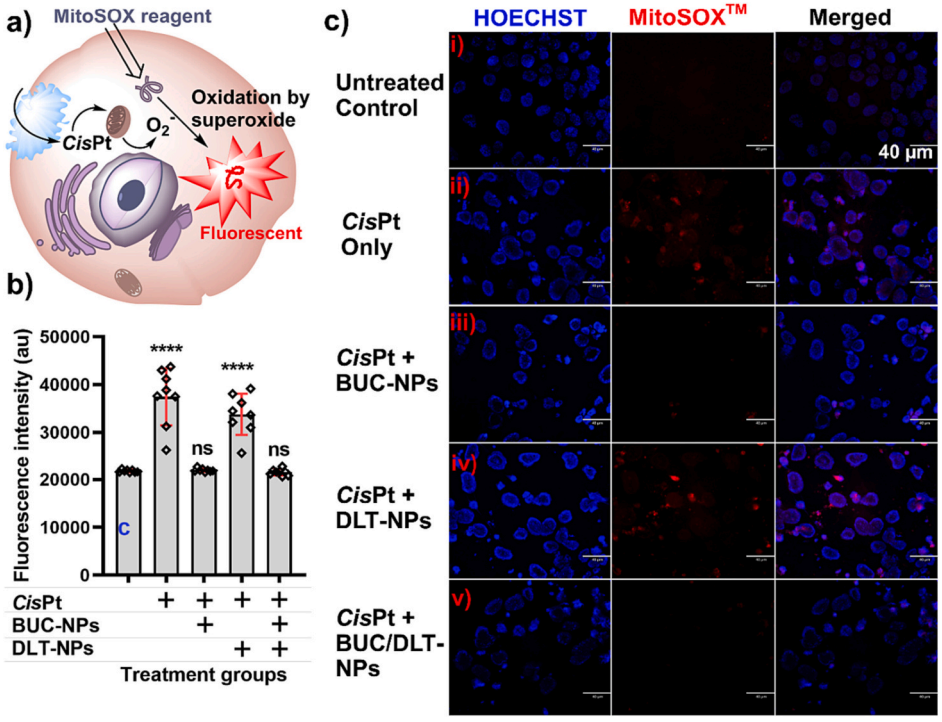

Fig. 8. The MitoSOX™ assay for the detection of *Cis*Pt-induced superoxide generation in mitochondria of HEI-OC1 cells. **(a) Mechanism of MitoSOX assay:** The nonfluorescent MitoSOX reagent reacts with mitochondrial superoxide and produces red fluorescence. This fluorescence generation can be noted as confirmation of mitochondrial superoxide generation in the cell referred to as oxidative stress of the cells. **(b) Quantitative comparison of fluorescence generation:** The graph shows fluorescence intensities of MitoSOX in various treatment groups. The higher fluorescence in a group can be directly correlated with the higher superoxide generation in the respected group. All treatment groups (except BUC-NPs alone and BUC/DLT-NPs treated) showed significantly higher fluorescence intensities compared to the untreated control group (denoted by the 'c'). The combined formulation of BUC/DLT-NPs has significant capability to quench superoxide which was generated by *Cis*Pt induction. (The groups were analyzed using one-way ANOVA using Šidák's multiple comparison post-hoc test. '$n = 8$', Asterisks: **** $P < 0.0001$; ns = not significant). **(c) Fluorescence microscopy imaging of various treatment groups after MitoSOX staining:** The fluorescence microscopy images of various groups to observe the fluorescence generation in the HEI-OC1 cells associated with the production of mitochondrial superoxide. The first column shows the HOECHST 33342-stained nuclei of each cell irrespective of the presence and absence of mitochondrial superoxide. The second column (MitoSOX™) shows red fluorescence where the higher fluorescence is associated with higher superoxide production. The third column shows merged images. (Scale 40 µm). Here, (i) the untreated cells did not show much fluorescence suggest the absence of superoxide, (ii) *Cis*Pt-only treated cells show significantly high fluorescence suggest the production of superoxide, (iii) BUC-NPs treated cells show significant inhibition of superoxide (low fluorescence) after subsequent treatment of *Cis*Pt, (iv) DLT-NPs treated cells with subsequent *Cis*Pt treatment group show a significant superoxide generation, (v) BUC/DLT-NPs treated cells with subsequent *Cis*Pt treatment group did not show significant superoxide generation (no significant MitoSOX fluorescence). Therefore, the treatment groups having BUC (BUC-NPs and BUC/DLT-NPs) showed significant superoxide scavenging capability, generated from mitochondria by *Cis*Pt-induction. (For interpretation of the references to colour in this figure legend, the reader is referred to the web version of this article.)

caspase inhibitor peptide sequence (DEVD: aspartic acid-glutamic acid-valine-aspartic acid); (3) a moiety responsible for irreversible binding (FMK: fluoromethyl ketone). Mechanistically, after cell internalization, the FLICA covalently attaches to activated caspase 3/7 proteins and the unbound FLICA washed out from the cells. FLICA which is attached to the activated caspase 3/7 shows green fluorescence that represents the confirmation of caspase 3/7 activation (Fig. 9**a**) [58]. To understand the effect of developed formulations on *Cis*Pt-induced caspase 3/7 activation, FLICA assay was performed. The results suggested that the cells that were treated with BUC-based NPs (BUC-NPs and BUC/DLT-NPs) did not show significant fluorescence. However, the cells that were treated with DLT-NPs only showed significant fluorescence similar to *Cis*Pt treated control (Fig. 9**b**). The results were further confirmed by fluorescence microscopy which confirmed that the BUC is highly responsible for the inhibition of the caspase 3/7 activation in the *Cis*Pt-exposed HEI-OC1 cells (Fig. 9**c**). Caspase inhibition by developed BUC-entrapped NPs could be highly desirable for reduced *Cis*Pt-induced cytotoxicity and CIO, subsequently.

3.6.4. Determination of probable cytoprotective pathway using western blot analysis

P-38 mitogen-activated protein kinase (MAPK), AKT, and ERK signaling are the classic pathways to investigate the cytoprotective effect of BUC/DLT-NPs. The activation and/or down-regulation as pharmacological intervention of this pathway reflects the potential damage, protection, and/or survival mechanisms to prevent or ameliorate ototoxicity in the representative auditory cell line (HEI-OC1). It has been reported that the upregulation of phosphorylated P38 and phosphorylated AKT plays a crucial role in CIO prevention [59,60]. The western blot results shown in Fig. 10 have increased protein expression levels of p-P38 and p-AKT levels upon treatment with both BUC- and DLT-NPs alone or in combination. Interestingly, no significant changes in ERK proteins were observed. While these results corroborate the previous findings, we can speculate that our treatment regimen (NP formulations) shields the HEI-OC1 cells from *Cis*Pt-induced toxicity via P38 MAPK, AKT, and ERK signaling pathways. However, more studies with related pathways are needed to be carried out to confirm the associated molecular pathways for cytoprotective effect. Moreover, as we have observed, a better effect of the BUC-based formulation compared to DLT-based formulations. That might be because of the direct ROS scavenging

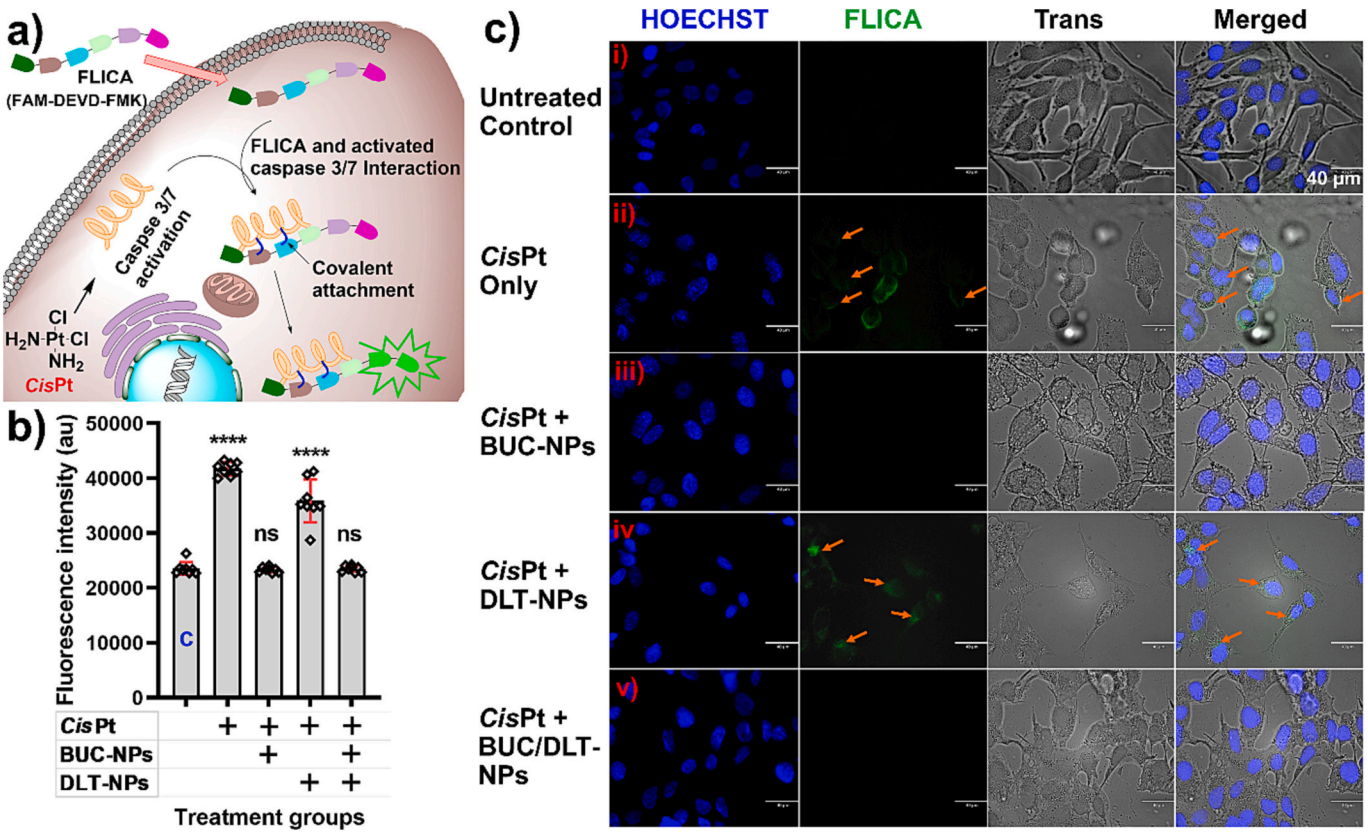

Fig. 9. The caspase 3/7 assay for the detection of *Cis*Pt-induced oxidative stress in HEI-OC1 cells. **(a) Mechanism of caspase 3/7 activation assay:** The conversion of nonfluorescent FLICA to fluorescently labeled into the cell cytoplasm by caspase 3/7 activation. FLICA which reached inside the cell first interacted with activated caspase 3/7, then subsequently covalently attached with it and produced green fluorescence. This fluorescence generation can be noted as confirmation of caspase 3/7 activation referred to as oxidative stress of the cells. **(b) Quantitative comparison of fluorescence generation:** The graph shows fluorescence intensities of FLICA in various treatment groups. The higher fluorescence in a group can be directly correlated with the higher caspase 3/7 activation in the respected group. All treatment groups except BUC-NPs alone and BUC/DLT-NPs treated showed significantly higher fluorescence intensities compared to the untreated control group (denoted by the 'c'). ('$n = 8$', Asterisks: **** $P < 0.0001$; ns = not significant). **(c) Fluorescence microscopy imaging of caspase 3/7 assay treatment groups:** The fluorescence microscopy images of various groups to observe the fluorescence generation in the HEI-OC1 cells associated with the activation of caspase 3/7. The first column shows the HOECHST 33342-stained nuclei of each cell irrespective of oxidatively stressed or unstressed. The second column (FLICA) shows the fluorescence of a covalently attached fluorophore to the caspase 3/7 proteins (the higher fluorescence is associated with the presence of a higher concentration of caspase 3/7 proteins). The third column shows cells under transmittance light. The fourth column shows merged images. (Scale 40 µm). Here, (i) the untreated cells did not show much fluorescence suggest the inactivation of caspase 3/7, (ii) *Cis*Pt-only treated cells show significantly high fluorescence suggest activation of caspase 3/7, (iii) BUC-NPs treated cells did not show significant caspase 3/7 activation (low fluorescence) upon subsequent treatment of *Cis*Pt, (iv) DLT-NPs treated cells with subsequent *Cis*Pt treatment group show a significant caspase 3/7 activation (FLICA fluorescence), (v) BUC/DLT-NPs treated cells with subsequent *Cis*Pt treatment group did not show caspase 3/7 activation (no significant FLICA fluorescence). Thus, the BUC-NPs and BUC/DLT-NPs have significant capability to inhibit *Cis*Pt induced caspase 3/7 activation. (For interpretation of the references to colour in this figure legend, the reader is referred to the web version of this article.)

capability of BUC.

3.7. Preparation and characterization of NanoSensoGel formulation for efficient local delivery of NP preparations

3.7.1. Preparation of NanoSensoGel and its physical behavior at different temperatures

Although, BUC-NPs and BUC/DLT-NPs-based treatment regimens showed significant cytoprotective efficacy against *Cis*Pt-induced cytotoxicity in HEI-OC1 cells, their delivery in the inner ear is a limiting factor to achieving the desired effect toward CIO prevention. The lower retention of the NP preparations in the middle ear after the administration is the main concern because of the clearance of liquid formulations through the Eustachian tube [61]. Therefore, to achieve the efficient delivery of the developed NPs in the middle ear, the thermoresponsive gel formulation named NanoSensoGel was prepared by embedding the BUC-NPs and DLT-NPs in the mixture of P407 (24% *w/v*), P188 (15% w/v) and C940 (0.1% w/v). The developed NanoSensoGel was found to be in a sol state at a temperature below 30 °C and able to pass through a 25-gauze needle very easily. The formulation converted to a gel state at a precise temperature above 33 °C (Fig. 11**a**). The transition from sol to gel state makes the formulation to be highly stable at body temperature which is essential for its long-term stability in the middle ear after the administration. The conversion of the formulation from sol to gel state in the middle ear restrains its washout through the Eustachian tube. Thus, it is expected that long-term release could be achieved by administering the drugs using the NanoSensoGel formulation. At higher temperatures, the micellar arrangement of the polymeric units due to hydrophobic interactions between polymeric chains might be responsible for the conversion of the sol to gel state [62] (Fig. 11**b**). To confirm the arrangement of polymeric units at the higher temperature the developed NanoSensoGel formulation was carefully characterized using scanning electron microscopy (Fig. 11**c**). It was observed that in the sol state, the polymeric units of NanoSensoGel showed random patterns which might be responsible for its fluid state with low viscosity (Fig. 11**c 'i' & 'ii'**). However, at higher temperatures, the polymeric units of the NanoSensoGel showed well-arranged patterns (honeycomb type) that might be responsible for their conversion of hard gel without

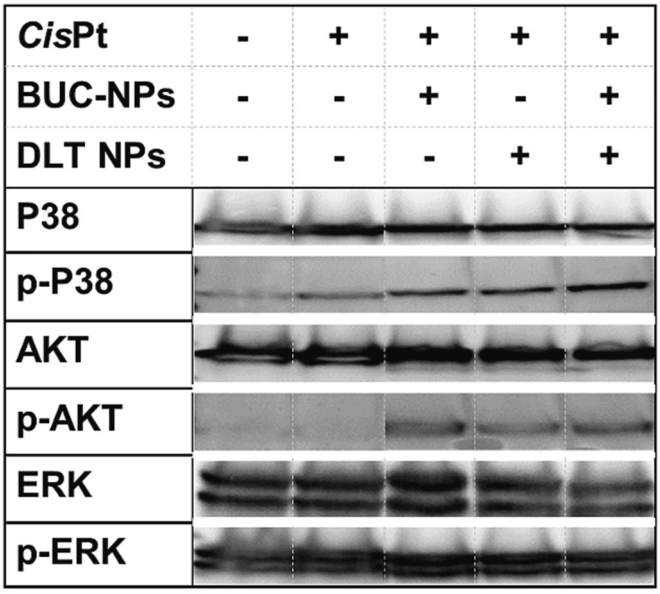

Fig. 10. The western blot analysis of the samples after treatment with developed NP formulations using antibodies associated with P38 MAPK, AKT, and ERK signaling pathways. (Note: The first two columns were merged with three columns associated with designated desired treatment groups from the same blot. The undesired treatment groups were trimmed from the blots).

losing the water and entrapped NPs (Fig. 11**c 'iii' & 'iv'**). The study suggested that the temperature above 33 °C was responsible for the arrangement of the molecules in an organized micellar pattern which was responsible for sol to gel conversion of the hydrogel at higher temperatures and further stabilization.

3.7.2. In vitro release kinetics of the BUC and DLT from NanoSensoGel

The release of the drugs from the hydrogel formulation is important to achieve the desired effect at the target site. Therefore, the release study of BUC and DLT from NanoSensoGel was performed in PBS buffer (pH 7.4) using well inserts and 24 well plate (Fig. 11**d 'i' & 'ii'**). The release of BUC/DLT from NanoSensoGel formulation was compared with free BUC/DLT-Gel formulation. It was observed that both free and NP-encapsulated BUC/DLT showed similar release patterns, however, the release rate of NP-encapsulated BUC/DLT was found to be slower than the free drugs. The maximum of 54 and 51% release of BUC and DLT, respectively was observed from NanoSensoGel in one week (168 h). Nevertheless, ~100% release of BUC and DLT was observed from free BUC/DLT-Gel within 48 h (Fig. 11**e i & ii**). The release mechanism was determined by fitting the release data with the Korsmeyer-Peppas model (KP-model). It was observed that the release percentage values well fit with the KP model (Fig. 11**f**). It was observed the 'n' (release mechanism exponent) values of BUC and DLT release from Free BUC/DLT-Gel were found to be between 0.5 and 1 ($0.5 < n < 1$) which suggests the non-Fickian diffusion. However, the 'n' values for BUC and DLT release from NanoSensoGel formulations were found to be <0.5 which suggests Fickian diffusion (Table 1) [63]. The Fickian diffusion of BUC and DLT from the NanoSenoGel can be corroborated by the diffusion of spherical NPs from the gel into the release media (**SI Fig. S7**). In free BUC/DLT-Gel formulations, rapid release at first was observed which trails off over time. Therefore, the release mechanism of free BUC and DLT from developed formulations was followed by the combination of swelling of polymeric hydrogels and diffusion simultaneously [64]. However, The release from NanoSensoGel formulation might depend on the excretion of BUC- and DLT-NPs into the receiving buffer. To confirm the excretion of the NPs, the concentration of released NPs in the buffer was determined using NTA. It was observed that the excretion of the NPs in the release media was significantly faster up to 48 h., then it was marginal up to 168 h (**SI Fig. S7**). In a simultaneous experiment, the stability of BUC and DLT in the NanoSensoGel formulation was determined at 25 and 37 °C storage conditions for 8 consecutive days. There was no significant difference in the concentrations of BUC and DLT in NanoSensoGel formulation observed (Fig. 11g). Therefore, it can be confirmed that the encapsulated BUC and DLT were stable in the NanoSensoGel formulation at both 25 and 37 °C temperatures. The results suggested that the developed NanoSensoGel formulation was efficiently able to deliver BUC/DLT for a longer time compared to free drug hydrogel formulation. Therefore, the developed NanoSensoGel formulations could be highly beneficial for delivery of BUC/DLT in the inner ear to circumvent CIO.

3.7.3. The cytoprotective effect of NanoSensoGel upon CisPt-exposed HEI-OC1 cells

Furthermore, the cytoprotective ability of NanoSensoGel formulation against *Cis*Pt-induced toxicity was studied on HEI-OC1 cells. The cells were treated with NanoSensoGel, free BUC/DLT-Gel, BUC/DLT-NPs, and free BUC/DLT solution. The results suggested that the NanoSensoGel and BUC/DLT-NPs showed significant cytoprotective effects while the cells treated with free BUC/DLT-Gel and free BUC/DLT did not show significant growth (Fig. 11**h**). The results corroborate the findings of the previous section where we discussed the cytoprotective effect of NPs without gel. Therefore, it may be concluded that the NanoSensoGel formulation could play a significant role in the protection of CIO.

4. Conclusion

In this study, a biocompatible NanoSensoGel formulation combined with BUC and DLT-loaded ROS-responsive NPs in a thermo-responsive hydrogel matrix has been developed for sustained long-term inner ear drug delivery for prophylactic treatment of CIO and associated hearing loss. A ROS-responsive polymer has been successfully synthesized and characterized to assemble BUC- and DLT-loaded PPS-mPEG$_{2000}$-NPs (BUC- and DLT-NPs). The central composite design was run to optimize the nanoformulation achieving a high EE/ DL and small nanoparticle size with a low PDI. The nanoprecipitation method has been utilized to construct NPs with EE and DL of 55.54 ± 6.17 and 88.52 ± 3.78%, and 8.05 ± 0.77 and 13.13 ± 0.40%, respectively. The mean particle size of BUC- and DLT-NPs ranged between 95 and 150 nm with a PDI value <0.2. Several in vitro investigations of the nanoformulations confirmed their biocompatibility with HEI-OC1 cells and cytoprotective effect after *Cis*Pt exposure. The dual-drug combination NPs were able to protect HEI-OC1 cells because of the ROS and superoxide scavenging properties of BUC and apoptosis-induced effects of DLT established by the intracellular ROS, MitoSOX™, and Caspase 3/7 assays. These data confirmed that the combined formulation of BUC and DLT with enhanced efficiency could potentially establish the prophylactic treatment regimen for CIO. Furthermore, a thermo-responsive P407, P188, and C940-based hydrogel formulation was developed to serve as a drug reservoir at the site of administration and allowed the diffusion of the drug from the middle ear cavity to the cochlea via RWM. The composite NanoSensoGel formulation i.e., dual-drug NPs suspended in the hydrogel matrix provided a sustained in vitro release of both BUC and DLT for more than a week. The release kinetics fitted well with the Korsmeyer-Peppas model with n values <0.5 ($n < 0.5 < 1$) suggesting the Fickian release of the drug-loaded NPs from the NanoSensoGel. The rationally designed dual bio-responsive approach present here illuminates the ROS-responsive drug release and the thermo-responsive conversion mechanism provides enhanced injectability at the inner ear site with a sustained long-term drug release profile. Overall, based on the drug delivery attributes, biocompatibility, and in vitro testing results elucidated above, the NanoSensoGel formulation developed in this study showed a great potential to prevent CIO and associated hearing loss. Future investigations are required such as the preclinical testing in various ototoxicity animal models to confirm the therapeutic potential of this novel NanoSensoGel

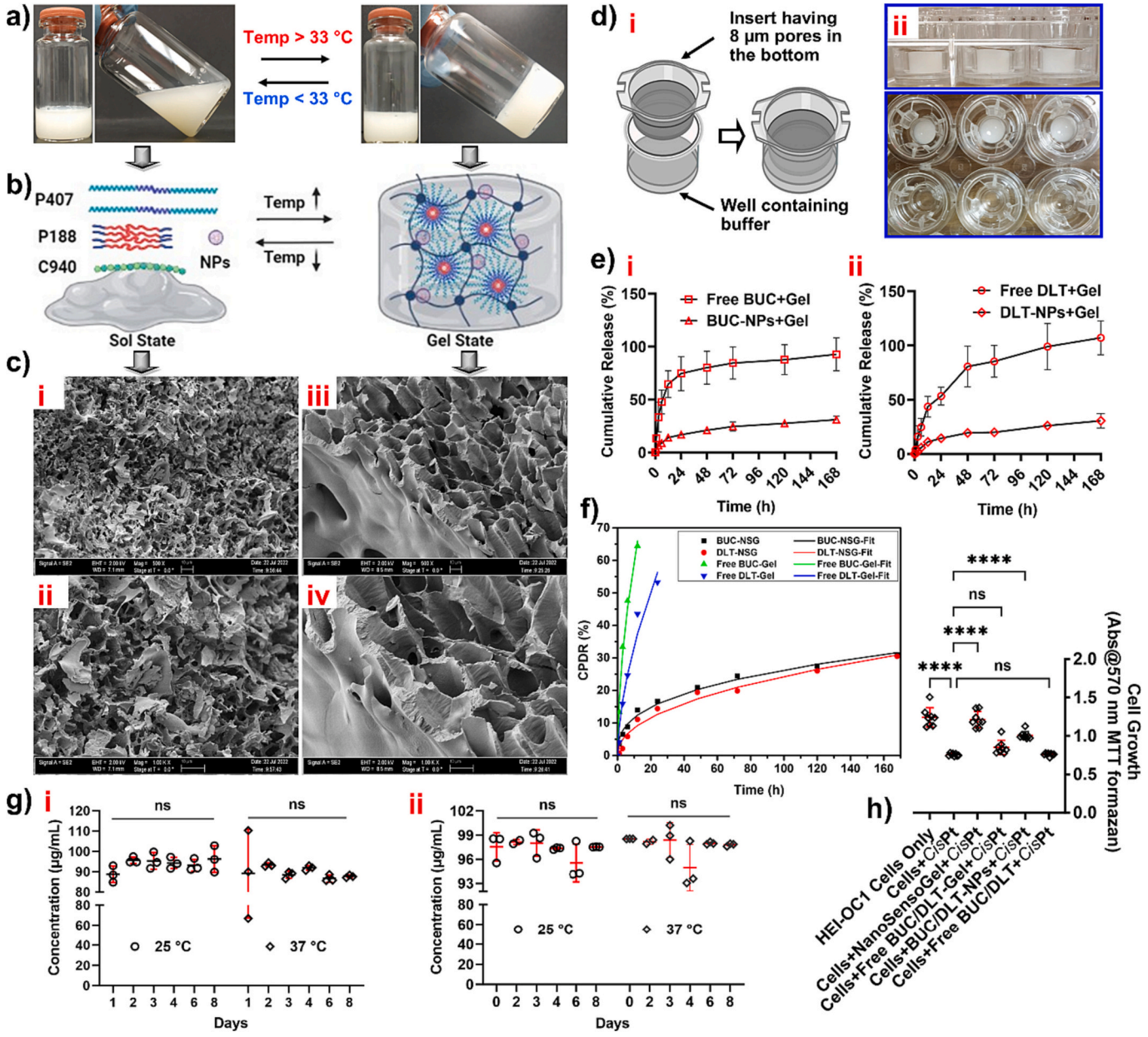

Fig. 11. Synthesis and characterization of NanoSensoGel formulation. **(a)** Figure showing the effect of temperature on the NanoSensoGel formulation. The formulation's sol state converts to gel state at/above 33 °C, while below 33 °C the formulation remains in the sol state. **(b)** The schematic presentation of components of the NanoSensoGel and the appearance of sol-gel states at varying temperatures. At temperature below 33 °C, the gel is present in a flowing sol state while at a higher temperature, the formulation components are arranged in the micellar structure and form a nonflowing gel state (created using Biorender.com). **(c)** SEM images of the NanoSensoGel. (i and ii) SEM images of hydrogel were kept below 30 °C at sol state then snap-freeze using liquid nitrogen at −196 °C and lyophilized subsequently. The sample observed under the SEM shows un-arranged pattern in the structure (scale 10 µm). (iii and iv) SEM images of hydrogel were kept at 34 °C gel state then snap-freeze and lyophilized subsequently. The sample observed under the SEM showed a well-arranged honeycomb-type pattern in the structure (scale 10 µm). **(d)** 'i'; the pictorial representation of well-insert that was used for the drug release study from the hydrogel (created using Biorender.com). 'ii'; the pictures captured after setting up the release experiments. The upper picture shows the side view of wells containing NanoSensoGel formulation in the insert. The lower picture shows the upper view of the NanoSensoGel and free drugs containing gel. **(e)** Graphs 'i and ii' are showing the percent release of BUC and DLT from NanoSensoGel and free BUC/DLT-Gel, respectively ($n = 3$). **(f)** The graph shows the fitting of cumulative percent drug release (CPDR) data with the Korsmeyer-Peppas Model. Here: BUC-NSG = BUC released from NanoSensoGel; DLT-NSG = DLT released from NanoSensoGel; Free-BUC-Gel = BUC released from free BUC/DLT-Gel formulation; Free-DLT-Gel = DLT released from free BUC/DLT-Gel formulation. **(g)** Graphs 'i and ii' are show respective stability of BUC and DLT in the hydrogel kept at 25 and 37 °C. (The data were analyzed using two-way ANOVA using Šidák's multiple comparison post-hoc test. 'n = 3′, ns = not significant). **(h)** The graph showing the cytoprotective effect of NanoSensoGel compared with free BUC/DLT-Gel, BUC/DLTNPs, and free BUC/DLT solution after the cell (HEI-OC1) exposed to *Cis*Pt (The data were analyzed using one-way ANOVA using Šidák's multiple comparison post-hoc test. '$n = 8$′, Asterisks: **** $P < 0.0001$, ns = not significant).

Table 1
The Korsmeyer-Peppas model fit values of the BUC and DLT release from the developed formulations.

Model parameters	Free BUC/DLT-Gel		NanoSensoGel	
	BUC	DLT	BUC	DLT
K_1	17.20	8.69	5.16	2.96
n	0.54	0.59	0.35	0.46
R^2	0.9951	0.9857	0.9954	0.9884

formulation for CIO and other hearing loss diseases such as age-related, noise-induced, sensorineural hearing loss, and other types of drug-induced ototoxicity.

CRediT authorship contribution statement

Neeraj S. Thakur: Conceptualization, Investigation, Methodology, Validation, Visualization, Writing – original draft, Formal analysis, Resources. **Iulia Rus:** Formal analysis, Validation, Investigation. **Ethan Sparks:** Investigation, Validation, Visualization. **Vibhuti Agrahari:** Conceptualization, Data curation, Funding acquisition, Methodology, Project administration, Resources, Supervision, Visualization, Writing – review & editing.

Declaration of competing interest

Neeraj S. Thakur and Vibhuti Agrahari declare the following competing financial interest(s): A US patent has been applied for the majority of this research work under application no. 63/509,823.

Data availability

Data will be made available on request.

Acknowledgements

This study was supported by awards from the Presbyterian Health Foundation (PHF) New Investigator Seed Grant Program, Capita Foundation Auditory Research (CFAR) Grant, and the National Cancer Institute 5P20CA253258-04 1/2 Cherokee Nation/OSU and SCC Collaborative Partnership for Cancer Research We thank Dr. A. D. Joshi for the fluorescence microscopy facility and helped with the western blot characterizations; Dr. A. W. Burgett for NMR facility; and Dr. V. Awasthi for DLS and Lyophilization facilities at the College of Pharmacy, University of Oklahoma Health Sciences Center (OUHSC) . The authors would like to thank Drs. R. D. Kopke and M. B. West from the Hough Ear Institute (HEI), Oklahoma City, for providing the HEI-OC1 Cell lines. The authors acknowledge the Samuel Roberts Noble Microscopy Laboratory at the University of Oklahoma for electron microscopy, and the Stephenson Molecular Imaging Core for NTA analysis at OUHSC.

Appendix A. Supplementary data

Supplementary data to this article can be found online at https://doi.org/10.1016/j.jconrel.2024.02.005.

References

[1] S. Ghosh, Cisplatin: The first metal based anticancer drug, *Bioorganic chemistry* 88 (2019): 102925, doi: 10.1016/j.bioorg.2019.102925.
[2] Q. Tang, X. Wang, H. Jin, Y. Mi, L. Liu, M. Dong, Y. Chen, Z. Zou, Cisplatin-induced ototoxicity: updates on molecular mechanisms and otoprotective strategies, Eur. J. Pharm. Biopharm. 163 (2021) 60–71, https://doi.org/10.1016/j.ejpb.2021.03.008.
[3] X. Wang, Y. Zhou, D. Wang, Y. Wang, Z. Zhou, X. Ma, X. Liu, D. Yaodong, Cisplatin-induced ototoxicity: From signaling network to therapeutic targets, Biomedicine & Pharmacotherapy 157 (2023) 114045, https://doi.org/10.1016/j.biopha.2022.114045.
[4] E. Gentilin, E. Simoni, M. Candito, D. Cazzador, L. Astolfi, Cisplatin-induced ototoxicity: updates on molecular targets, Trends Mol. Med. 25 (2019) 1123–1132, https://doi.org/10.1016/j.molmed.2019.08.002.
[5] B. Nan, Z. Zhao, K. Jiang, X. Gu, H. Li, X. Huang, Astaxanthine attenuates cisplatin ototoxicity in vitro and protects against cisplatin-induced hearing loss in vivo, Acta Pharm. Sin. B 12 (2022) 167–181, https://doi.org/10.1016/j.apsb.2021.07.002.
[6] T. Harao, A. Yamada, M. Kinoshita, S. Kamimura, H. Moritake, Prevention of cisplatin-induced hearing-loss by sodium thiosulfate in medulloblastoma, Pediatr. Int. 62 (2020) 1204–1206, https://doi.org/10.1111/ped.14271.
[7] R.A. Hazlitt, J. Min, J. Zuo, Progress in the development of preventative drugs for cisplatin-induced hearing loss, J. Med. Chem. 61 (2018) 5512–5524, https://doi.org/10.1021/acs.jmedchem.7b01653.
[8] D.R. Freyer, P.R. Brock, K.W. Chang, L.L. Dupuis, S. Epelman, K. Knight, D. Mills, R. Phillips, E. Potter, D. Risby, P. Simpkin, M. Sullivan, S. Cabral, P.D. Robinson, L. Sung, Prevention of cisplatin-induced ototoxicity in children and adolescents with cancer: a clinical practice guideline, Lancet Child Adolesc. Heal. 4 (2020) 141–150, https://doi.org/10.1016/S2352-4642(19)30336-0.
[9] FDA Approves Sodium Thiosulfate To Reduce The Risk Of Ototoxicity Associated With Cisplatin In Pediatric Patients With Localized, Non-Metastatic Solid Tumors | FDA. https://www.fda.gov/drugs/resources-information-approved-drugs/fda-approves-sodium-thiosulfate-reduce-risk-ototoxicity-associated-cisplatin-pediatric-patients, 2024. (Accessed 23 November 2022).
[10] Sodium Thiosulfate (Intravenous Route) Side Effects - Mayo Clinic. https://www.mayoclinic.org/drugs-supplements/sodium-thiosulfate-intravenous-route/side-effects/drg-20066076?p=1, 2024 (accessed August 26, 2023).
[11] B.I. Drögemöller, G.E.B. Wright, C. Lo, T. Le, B. Brooks, A.P. Bhavsar, S.R. Rassekh, C.J.D. Ross, B.C. Carleton, Pharmacogenomics of cisplatin-induced ototoxicity: successes, shortcomings, and future avenues of research, Clin. Pharmacol. Ther. 106 (2019) 350–359, https://doi.org/10.1002/cpt.1483.
[12] L.D. Horwitz, Bucillamine: a potent thiol donor with multiple clinical applications, Cardiovasc. Drug Rev. 21 (2003) 77–90, https://doi.org/10.1111/j.1527-3466.2003.tb00107.x.
[13] S.J. Kim, J.H. Hur, C. Park, H.J. Kim, G.S. Oh, J.N. Lee, S.J. Yoo, S.K. Choe, H.S. So, D.J. Lim, S.K. Moon, R. Park, Bucillamine prevents cisplatin-induced ototoxicity through induction of glutathione and antioxidant genes, Exp. Mol. Med. 47 (2015), https://doi.org/10.1038/emm.2014.112.
[14] B. Bhandary, A. Marahatta, H.R. Kim, H.J. Chae, An involvement of oxidative stress in endoplasmic reticulum stress and its associated diseases, Int. J. Mol. Sci. 14 (2013) 434–456, https://doi.org/10.3390/ijms14010434.
[15] T.R. Van de Water, R.N. Abi-Hachem, A. Zine, The injured cochlea as a target for inflammatory processes, initiation of cell death pathways and application of related otoprotective strategies, Recent Pat. CNS Drug Discov. 5 (2010) 147–163, https://doi.org/10.2174/157488910791213121.
[16] J.G. Naples, K. Parham, Cisplatin-induced ototoxicity and the effects of Intratympanic diltiazem in a mouse model, Otolaryngol. - Head Neck Surg. (United States). 154 (2016) 144–149, https://doi.org/10.1177/0194599815606704.
[17] C. Jaudoin, F. Agnely, Y. Nguyen, E. Ferrary, A. Bochot, Nanocarriers for drug delivery to the inner ear: physicochemical key parameters, biodistribution, safety and efficacy, Int. J. Pharm. 592 (2021), https://doi.org/10.1016/j.ijpharm.2020.120038.
[18] V. Agrahari, V. Agrahari, A.K. Mitra, Inner ear targeted drug delivery: what does the future hold? Ther. Deliv. 8 (2017) 179–184, https://doi.org/10.4155/tde-2017-0001.
[19] J. Hao, S.K. Li, Inner ear drug delivery: recent advances, challenges, and perspective, Eur. J. Pharm. Sci. 126 (2019) 82–92, https://doi.org/10.1016/j.ejps.2018.05.020.
[20] L. Li, T. Chao, J. Brant, B. O'Malley, A. Tsourkas, D. Li, Advances in nano-based inner ear delivery systems for the treatment of sensorineural hearing loss, Adv. Drug Deliv. Rev. 108 (2017) 2–12, https://doi.org/10.1016/j.addr.2016.01.004.
[21] H. Staecker, M. Morelock, T. Kramer, P. Chrbolka, J.H. Ahn, T. Meyer, Safety of repeated-dose Intratympanic injections with AM-101 in acute inner ear tinnitus, Otolaryngol. - Head Neck Surg. (United States). 157 (2017) 478–487, https://doi.org/10.1177/0194599817711378.
[22] X. An, D. Zha, Development of nanoparticle drug-delivery systems for the inner ear, Nanomedicine. 15 (2020) 1981–1993, https://doi.org/10.2217/nnm-2020-0198.
[23] Z. Zhao, Z. Han, K. Naveena, G. Lei, S. Qiu, X. Li, T. Li, X. Shi, W. Zhuang, Y. Li, Y. Qiao, H. Liu, ROS-responsive nanoparticle as a Berberine carrier for OHC-targeted therapy of noise-induced hearing loss, ACS Appl. Mater. Interfaces 13 (2021) 7102–7114, https://doi.org/10.1021/acsami.0c21151.
[24] J. Gu, X. Wang, Y. Chen, K. Xu, D. Yu, H. Wu, An enhanced antioxidant strategy of astaxanthin encapsulated in ROS-responsive nanoparticles for combating cisplatin-induced ototoxicity, J. Nanobiotechnology. 20 (2022), https://doi.org/10.1186/s12951-022-01485-8.
[25] S.A. Lajud, D.A. Nagda, P. Qiao, N. Tanaka, A. Civantos, R. Gu, Z. Cheng, A. Tsourkas, B.W. O'Malley, D. Li, A novel chitosan-hydrogel-based nanoparticle delivery system for local inner ear application, Otol. Neurotol. 36 (2015) 341–347, https://doi.org/10.1097/MAO.0000000000000445.
[26] S.J. Buwalda, K.W.M. Boere, P.J. Dijkstra, J. Feijen, T. Vermonden, W.E. Hennink, Hydrogels in a historical perspective: from simple networks to smart materials, J. Control. Release 190 (2014) 254–273, https://doi.org/10.1016/j.jconrel.2014.03.052.
[27] C. Woghiren, S. Steinf, B. Sharma, Protected thiol-polyethylene glycol: a new activated polymer for reversible protein modification, Bioconjug. Chem. 4 (1993) 314–318, https://doi.org/10.1021/bc00023a002.

[28] A. Napoli, N. Tirelli, G. Kilcher, J.A. Hubbell, New synthetic methodologies for amphiphilic multiblock copolymers of ethylene glycol and propylene sulfide, Macromolecules. 34 (2001) 8913–8917, https://doi.org/10.1021/ma0108057.
[29] Y. Fu, W.J. Kao, In situ forming poly(ethylene glycol)-based hydrogels via thiol-maleimide Michael-type addition, J. Biomed. Mater. Res. - Part A. 98 A (2011) 201–211, https://doi.org/10.1002/jbm.a.33106.
[30] S. Cerritelli, D. Velluto, J.A. Hubbell, PEG-SS-PPS: reduction-sensitive disulfide block copolymer vesicles for intracellular drug delivery, Biomacromolecules. 8 (2007) 1966–1972, https://doi.org/10.1021/bm070085x.
[31] K.S. Yadav, K.K. Sawant, Modified nanoprecipitation method for preparation of cytarabine-loaded PLGA nanoparticles, AAPS PharmSciTech 11 (2010) 1456–1465, https://doi.org/10.1208/s12249-010-9519-4.
[32] N.S. Thakur, J. Bhaumik, S. Kirar, U.C. Banerjee, Development of gold-based Phototheranostic Nanoagents through a bioinspired route and their applications in photodynamic therapy, ACS Sustain. Chem. Eng. 5 (2017) 7950–7960, https://doi.org/10.1021/acssuschemeng.7b01501.
[33] H. Kim, X. Xue, Detection of total reactive oxygen species in adherent cells by 2′,7′-dichlorodihydrofluorescein diacetate staining, J. Vis. Exp. 2020 (2020) 1–5, https://doi.org/10.3791/60682.
[34] H.S. So, H.J. Kim, J.H. Lee, J.H. Lee, S.Y. Park, C. Park, Y.H. Kim, J.K. Kim, K. M. Lee, K.S. Kim, S.Y. Chung, W.C. Jang, S.K. Moon, H.T. Chung, R.K. Park, Flunarizine induces Nrf2-mediated transcriptional activation of heme oxygenase-1 in protection of auditory cells from cisplatin, Cell Death Differ. 13 (2006) 1763–1775, https://doi.org/10.1038/sj.cdd.4401863.
[35] J. Chen, R. Zhou, L. Li, B. Li, X. Zhang, J. Su, Mechanical, rheological and release behaviors of a poloxamer 407/poloxamer 188/carbopol 940 thermosensitive composite hydrogel, Molecules. 18 (2013) 12415–12425, https://doi.org/10.3390/molecules181012415.
[36] E. Engleder, C. Honeder, J. Klobasa, M. Wirth, C. Arnoldner, F. Gabor, Preclinical evaluation of thermoreversible triamcinolone acetonide hydrogels for drug delivery to the inner ear, Int. J. Pharm. 471 (2014) 297–302, https://doi.org/10.1016/j.ijpharm.2014.05.057.
[37] R.W. Korsmeyer, R. Gurny, E. Doelker, P. Buri, N.A. Peppas, Mechanisms of solute release from porous hydrophilic polymers, Int. J. Pharm. 15 (1983) 25–35, https://doi.org/10.1016/0378-5173(83)90064-9.
[38] G.M. Kalinec, C. Park, P. Thein, F. Kalinec, Working with auditory HEI-OC1 cells, J. Vis. Exp. 2016 (2016) 1–10, https://doi.org/10.3791/54425.
[39] C. Sardo, T. Mencherini, C. Tommasino, T. Esposito, P. Russo, P. Del Gaudio, R. P. Aquino, Inulin-g-poly-D,L-lactide, a sustainable amphiphilic copolymer for nano-therapeutics, Drug Deliv. Transl. Res. 12 (2022) 1974–1990, https://doi.org/10.1007/s13346-022-01135-4.
[40] M.J. Mitchell, M.M. Billingsley, R.M. Haley, M.E. Wechsler, N.A. Peppas, R. Langer, Engineering precision nanoparticles for drug delivery, Nat. Rev. Drug Discov. 20 (2021) 101–124, https://doi.org/10.1038/s41573-020-0090-8.
[41] B. Liu, S. Thayumanavan, Mechanistic investigation on oxidative degradation of ROS-responsive Thioacetal/Thioketal moieties and their implications, Cell Reports Phys. Sci. 1 (2020) 100271, https://doi.org/10.1016/j.xcrp.2020.100271.
[42] G. Rajpal, P. Arvan, Disulfide bond formation, Handb. Biol. Act. Pept. (2013) 1721–1729, https://doi.org/10.1016/B978-0-12-385095-9.00236-0.
[43] N.S. Thakur, G. Patel, V. Kushwah, S. Jain, U.C. Banerjee, Facile development of biodegradable polymer-based nanotheranostics: hydrophobic photosensitizers delivery, fluorescence imaging and photodynamic therapy, J. Photochem. Photobiol. B Biol. 193 (2019) 39–50, https://doi.org/10.1016/j.jphotobiol.2019.02.007.
[44] K.S. Yadav, K.K. Sawant, Modified nanoprecipitation method for preparation of cytarabine-loaded PLGA nanoparticles, AAPS PharmSciTech 11 (2010) 1456–1465, https://doi.org/10.1208/s12249-010-9519-4.
[45] A.R. Studart, E. Amstad, L.J. Gauckler, Colloidal stabilization of nanoparticles in concentrated suspensions, Langmuir. 23 (2007) 1081–1090, https://doi.org/10.1021/la062042s.
[46] M.N. Gupta, I. Roy, How Corona formation impacts nanomaterials as drug carriers, Mol. Pharm. 17 (2020) 725–737, https://doi.org/10.1021/acs.molpharmaceut.9b01111.
[47] Y. Sun, S.Y. Lau, Z.W. Lim, S.C. Chang, F. Ghadessy, A. Partridge, A. Miserez, Phase-separating peptides for direct cytosolic delivery and redox-activated release of macromolecular therapeutics, Nat. Chem. 14 (2022) 274–283, https://doi.org/10.1038/s41557-021-00854-4.
[48] T.A. Kelf, V.K.A. Sreenivasan, J. Sun, E.J. Kim, E.M. Goldys, A.V. Zvyagin, Non-specific cellular uptake of surface-functionalized quantum dots, Nanotechnology. 21 (2010), https://doi.org/10.1088/0957-4484/21/28/285105.
[49] Y. Li, M. Kröger, W.K. Liu, Endocytosis of PEGylated nanoparticles accompanied by structural and free energy changes of the grafted polyethylene glycol, Biomaterials. 35 (2014) 8467–8478, https://doi.org/10.1016/j.biomaterials.2014.06.032.
[50] B. Yameen, W. Il Choi, C. Vilos, A. Swami, J. Shi, O.C. Farokhzad, Insight into nanoparticle cellular uptake and intracellular targeting, J. Control. Release 190 (2014) 485–499, https://doi.org/10.1016/j.jconrel.2014.06.038.
[51] N.S. Thakur, N. Mandal, G. Patel, S. Kirar, Y.N. Reddy, V. Kushwah, S. Jain, Y. N. Kalia, J. Bhaumik, U.C. Banerjee, Co-administration of zinc phthalocyanine and quercetin via hybrid nanoparticles for augmented photodynamic therapy, nanomedicine nanotechnology, Biol. Med. 33 (2021) 102368, https://doi.org/10.1016/j.nano.2021.102368.
[52] H.S. So, C. Park, H.J. Kim, J.H. Lee, S.Y. Park, J.H. Lee, Z.W. Lee, H.M. Kim, F. Kalinec, D.J. Lim, R. Park, Protective effect of T-type calcium channel blocker flunarizine on cisplatin-induced death of auditory cells, Hear. Res. 204 (2005) 127–139, https://doi.org/10.1016/j.heares.2005.01.011.
[53] A. Barzegar, A.A. Moosavi-Movahedi, Intracellular ROS protection efficiency and free radical-scavenging activity of curcumin, PLoS One 6 (2011) e26012, https://doi.org/10.1371/journal.pone.0026012.
[54] S.I. Dikalov, D.G. Harrison, Methods for detection of mitochondrial and cellular reactive oxygen species, antioxidants redox, Signal. 20 (2014) 372–382, https://doi.org/10.1089/ars.2012.4886.
[55] H.J. Kim, J.H. Lee, S.J. Kim, G.S. Oh, H.D. Moon, K.B. Kwon, C. Park, B.H. Park, H. K. Lee, S.Y. Chung, R. Park, H.S. So, Roles of NADPH oxidases in cisplatin-induced reactive oxygen species generation and ototoxicity, J. Neurosci. 30 (2010) 3933–3946, https://doi.org/10.1523/JNEUROSCI.6054-09.2010.
[56] R. Marullo, E. Werner, N. Degtyareva, B. Moore, G. Altavilla, S.S. Ramalingam, P. W. Doetsch, Cisplatin induces a mitochondrial-ros response that contributes to cytotoxicity depending on mitochondrial redox status and bioenergetic functions, PLoS One 8 (2013) e81162, https://doi.org/10.1371/journal.pone.0081162.
[57] J.G. Walsh, S.P. Cullen, C. Sheridan, A.U. Lüthi, C. Gerner, S.J. Martin, Executioner caspase-3 and caspase-7 are functionally distinct proteases, Proc. Natl. Acad. Sci. USA 105 (2008) 12815–12819, https://doi.org/10.1073/pnas.0707715105.
[58] M. Killinger, B. Veselá, M. Procházková, E. Matalová, K. Klepárník, A single-cell analytical approach to quantify activated caspase-3/7 during osteoblast proliferation, differentiation, and apoptosis, Anal. Bioanal. Chem. 413 (2021) 5085–5093, https://doi.org/10.1007/s00216-021-03471-9.
[59] Y. Zhang, Z. Lv, Q. He, Agmatine alleviates cisplatin-induced ototoxicity by activating PI3K/AKT signaling pathway, ENeuro. 9 (2022), https://doi.org/10.1523/ENEURO.0434-21.2022.
[60] D. Raj, B. Kraish, J. Martikainen, A. Podraza-Farhanieh, G. Kao, P. Naredi, Cisplatin toxicity is counteracted by the activation of the p38/ATF-7 signaling pathway in post-mitotic *C. elegan*, Nat. Commun. 14 (2023), https://doi.org/10.1038/s41467-023-38568-5.
[61] B. Szeto, H. Chiang, C. Valentini, M. Yu, J.W. Kysar, A.K. Lalwani, Inner ear delivery: challenges and opportunities, Laryngoscope Investig. Otolaryngol. 5 (2020) 122–131, https://doi.org/10.1002/lio2.336.
[62] A. Fakhari, M. Corcoran, A. Schwarz, Thermogelling properties of purified poloxamer 407, Heliyon. 3 (2017) 390, https://doi.org/10.1016/j.heliyon.2017.e00390.
[63] G. Choi, E.I. Fitriasari, C. Park, Electro-Mechanochemical gating of a metal-phenolic Nanocage for controlled guest-release self-powered patches and injectable gels, ACS Nano 15 (2021) 14580–14586, https://doi.org/10.1021/acsnano.1c04276.
[64] M. Fosca, J.V. Rau, V. Uskoković, Factors influencing the drug release from calcium phosphate cements, Bioact. Mater. 7 (2022) 341–363, https://doi.org/10.1016/j.bioactmat.2021.05.032.